
Kelvin Probe Force Microscopy in Nanoscience and Nanotechnology

4

Da Luo, Hao Sun, and Yan Li

Contents

1	Definition of the Topic	118
2	Overview	118
3	Introduction	118
4	Physical Background and Theory for Kelvin Probe Method	119
4.1	Fundamentals	119
4.2	Electric Force and Electric Force Gradient	121
4.3	AM-KPFM	122
4.4	FM-KPFM	124
4.5	KPFM Without Potential Feedback	126
5	KPFM Measurement	127
5.1	Lock-In Settings for KPFM Measurement	127
5.2	KPFM Resolution	131
5.3	KPFM Sensitivity	133
5.4	KPFM Repeatability	134
6	Applications of KPFM in Nanoscale Characterization	134
6.1	Surface Charge	134
6.2	Work Function and Doping Level	137
6.3	Charge Transfer	144
6.4	Field Effect Transistors	148
6.5	Atomic Resolution KPFM	151
	References	154

D. Luo (✉) • Y. Li (✉)

Beijing National Laboratory for Molecular Sciences, Key Laboratory for the Physics and Chemistry of Nanodevices, College of Chemistry and Molecular Engineering, Peking University, Beijing, China

e-mail: yanli@pku.edu.cn

H. Sun

Nano Surfaces Division, Bruker (Beijing) Scientific Technology Co., Ltd, Beijing, China

1 Definition of the Topic

Kelvin probe force microscopy (KPFM) is applicable to measure surface potential and work function in a localized nanoscale surface area. In this chapter, we describe the theory and measurement of KPFM and its applications in the characterization of inorganic nanostructure and nanomaterials.

2 Overview

We will focus on fundamentals of KPFM and its applications in inorganic nanostructures and nanomaterials, such as carbon nanotubes (CNTs), graphene, nanocrystals, Si-based nano-devices, and so on. We will review the physical background of Kelvin probe method for electrical measurement and then focus on the two kinds of KPFM methods: one is called amplitude modulation KPFM (AM-KPFM) and the other is called frequency modulation KPFM (FM-KPFM). We will also discuss a special method, KPFM without feedback, which is used to detect high voltage. Then, we will analyze how to realize above KPFM methods by instruments and the influencing factors which can affect KPFM resolution, accuracy, sensitivity, and repeatability. Finally, we will discuss the applications of KPFM in characterization of inorganic nanostructure and nanomaterials. We will mainly focus on five KPFM applications: surface charge detection, work function and doping level study, charge transfer study, field effect transistors, and atomic resolution KPFM.

3 Introduction

Kelvin probe method, first introduced by Lord Kelvin in 1898 [1], is used to measure the contact potential difference (CPD) between metals. In this method, an external voltage is applied to null the electrical field generated by CPD between two metal materials. However, the electrical field is not directly perceived through the senses and cannot be measured very easily. In 1932, Zisman introduced a vibrating reference surface to improve Kelvin probe method into an alternating current (AC) way [2]. The vibrating reference surface leads to capacitance change between two metal plates, which induce a small AC current that can be detected very easily. Although it is an easy way to use Kelvin method and can achieve ~ 1 mV resolution, the major disadvantage for this method is that only average surface potential of the whole metal plate can be obtained, that means one cannot get any local surface potential information at all. This method is only applicable to macroscopic measurement.

After the invention of scanning probe microscope (SPM), it is the first time Kelvin method can be down to nanoscale world and measuring local surface potential was possible. Kelvin probe force microscopy (KPFM) [3, 4], also called scanning Kelvin probe microscopy (SKPM) or scanning potential microscopy (SPoM),

was developed by Wickramasinghe et al. in 1991 [5] and maps local electrostatic potential at sample surfaces to provide information about material work function [6], electronic structure [7], doping level variations [8], and trapped charges [9], in applications ranging from organic photovoltaic research [10] to field effect transistor (FET) characterization [11]. KPFM has obvious advantages in electrical measurement. First of all, the scanning probe technique takes KPFM method into nanoscale, and the high-resolution local potential imaging becomes possible. Second, it is a quantitative method which can tell us the potential value.

In this chapter, we will discuss about KPFM principles and its applications in inorganic nanostructures and nanomaterials.

4 Physical Background and Theory for Kelvin Probe Method

4.1 Fundamentals

When two metals contact with each other, their Fermi energy levels will be brought to the same level, because the energy of the highest occupied energy levels is different. The Fermi level of a metal is a concept in quantum mechanics usually referring to the energy level of the highest occupied quantum state in a system of fermions at absolute zero temperature, where all states below are occupied and all above are empty. In this case, the fermions are electrons. We define the difference of energy between electrons in vacuum state and that at Fermi energy level as “work function.” So the metal which the Fermi energy level is higher has a lower work function; meanwhile, the one which the Fermi energy level is lower has a higher work function. In other words, higher work function means stronger electron binding. When two metal plates are connected to each other, the electrons will flow from the material which has lower work function to the material which has higher work function. The opposite charges are produced on these two metal plates, leading to CPD generation. An electric field can be detected if the potentials on the two metal plates are different. If we carefully adjust an external bias V_{CPD} , a compensatory potential, to nullify the electric field, at equilibrium, when the electric field is nulled, the applied bias is equal to the CPD and all surface charges are disappear. At this point, if the work function of one metal plate is known, suppose it is ϕ_1 here, one can easily get the work function of the other metal plate, that is, $\phi_2 = \phi_1 - eV_{CPD}$, where e is quantity of electric charge of one electron. All Kelvin probe methods are based on this concept and the only difference is the way to detect this charge-free state.

Figure 4.1 illustrates the basic concept of Kelvin probe method. Before two metals contact with each other, they have different Fermi energy levels (E_{F1} for metal 1 and E_{F2} for metal 2). Suppose E_V is the vacuum level, the energy difference between E_F and E_V is the “work function.” For $E_{F1} < E_{F2}$, we can get $\phi_1 > \phi_2$. If we connect the two metals, electrons in metal 2, which have higher energy, will flow to metal 1 and finally result in a state of equilibrium. In this state, metal 1 will be negative charged because it obtains more electrons, and metal 2 will be positive

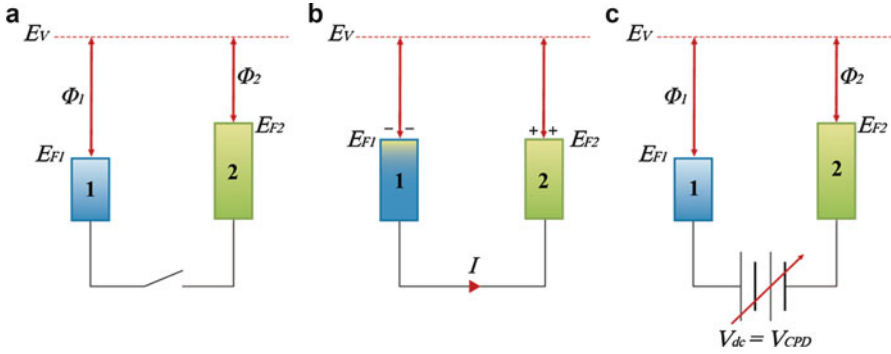


Fig. 4.1 Basic concepts of Kelvin probe method

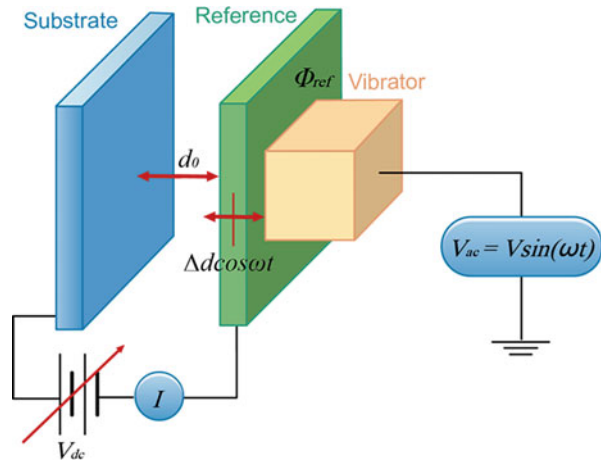


Fig. 4.2 AC Kelvin probe method experiment setup (Zisman)

charged because it loses some electrons. Kelvin probe method uses an adjustable external voltage source to null the surface charge on both metals. When all surface charges disappear, the external bias equals to the contact potential difference.

Zisman used a vibrating reference to improve the Kelvin probe method to an AC way [2]. In this setting, the way to detect charge-free state is to find the compensatory potential that can make the AC current between two metal plates zero. The experiment setup of Zisman is shown in Fig. 4.2. In this experiment setup, a metal plate is fixed (substrate in Fig. 4.2) and the other metal plate (Reference in Fig. 4.2, which has known work function) is vibrating at frequency ω . The mechanical oscillation induces the change of system capacitance, and thus an AC current will be detected if the potential difference between the two metal plates is not zero.

If the distance between the two metal plates is d_0 , when the reference plate is vibrating at frequency ω with amplitude Δd , the distance between the two metal plates can be given by

$$d = d_0 + \Delta d \cos \omega t \quad (4.1)$$

The modulated system capacitance C is given by

$$C(t) = \epsilon_0 \frac{A}{d_0 + \Delta d \cos \omega t} \quad (4.2)$$

where A is the area of metal plate and ϵ_0 is the dielectric constant of the free space. For $\Delta d \ll d_0$, Eq. 4.2 can be rewritten by

$$C(t) = \epsilon_0 \frac{A}{d_0} \left(1 - \frac{\Delta d}{d_0} \cos \omega t \right) \quad (4.3)$$

If we note the CPD between the two plates as ΔV , and apply a DC compensatory voltage V_{CPD} to nullify the CPD, the surface charge Q on the metal plates is given by

$$Q(t) = C(t)(\Delta V - V_{CPD}) \quad (4.4)$$

Thus, the current $i(t)$ between the two metal plates is

$$i(t) = \frac{\partial Q(t)}{\partial t} = -\epsilon_0 \frac{A}{d_0^2} \omega (\Delta V - V_{CPD}) \Delta d \sin \omega t \quad (4.5)$$

When $V_{CPD} = \Delta V$, $i(t)$ goes to zero.

4.2 Electric Force and Electric Force Gradient

Let us start from a simple model: a capacitor composed by two metal plates.

If charge $+Q$ is on a metal plate, whose area is A , according to Gauss's law, the electric field E_+ can be given by

$$E_+ = \frac{\sigma}{2\epsilon_0} \quad (4.6)$$

where σ is areal density of the electrical charge, equals to Q divided by area A .

In similar fashion, if charge $-Q$ is on a metal plate, the electric field E_- also can be got easily

$$E_- = \frac{\sigma}{2\epsilon_0} \quad (4.7)$$

When we put the two metal plates together to make a capacitor, the electric field outside the capacitor becomes zero and that between the two plates becomes

$$E = E_+ + E_- = \frac{\sigma}{\epsilon_0} = \frac{Q}{A\epsilon_0} \quad (4.8)$$

If the potential difference between the two metal plates is ΔV , it can be written as

$$\Delta V = Ed = \frac{Qd}{\epsilon_0 A} \quad (4.9)$$

where d is the distance of the two metal plates. Thus, the system capacitance C is

$$C = \frac{Q}{\Delta V} = \frac{\epsilon_0 A}{d} \quad (4.10)$$

The derivative of capacitance is given by

$$\left[\frac{\partial C}{\partial z} \right]_{z=d} = -\frac{\epsilon_0 A}{d^2} \quad (4.11)$$

Consequently, the electric force (attractive) between the two metal plates is

$$F = -\frac{1}{2}QE = \frac{1}{2} \left(\frac{\epsilon_0 A}{d^2} \right) (\Delta V)^2 \quad (4.12)$$

According to Eq. 4.11, Eq. 4.12 can be rewritten as

$$F = -\frac{1}{2} \frac{\partial C}{\partial z} (\Delta V)^2 \quad (4.13)$$

So the electric force gradient between the two metal plates is

$$\frac{\partial F}{\partial z} = -\frac{1}{2} \frac{\partial^2 C}{\partial z^2} (\Delta V)^2 \quad (4.14)$$

Equations 4.13 and 4.14 are the key results for parallel-plate condenser model.

In KPFM, a conductive probe and a conductive sample form the two plates of the plate condenser model. The electric force and electric force gradient can be expressed as exactly the same equation as Eqs. 4.13 and 4.14.

4.3 AM-KPFM

In AM-KPFM, an AC bias with frequency ω_m and amplitude V_{ac} , superimposed on a DC bias V_{dc} , is applied between tip and sample. An oscillating electric force, according to Eq. 4.13, is generated between tip and sample, which can be written as

$$F_e = -\frac{1}{2} \frac{\partial C}{\partial z} \left[V_{dc} - \Delta V + V_{ac} \sin(\omega_m t) \right]^2 \quad (4.15)$$

where ΔV is the CPD between tip and sample.

The above equation yields the following three components of the electric force, one at DC, that is,

$$F_{dc} = -\frac{1}{2} \frac{\partial C}{\partial z} \left[(V_{dc} - \Delta V)^2 + \frac{1}{2} V_{ac}^2 \right] \quad (4.16)$$

the second one at ω_m

$$F_\omega = -\frac{\partial C}{\partial z} (V_{dc} - \Delta V) V_{ac} \sin(\omega_m t) \quad (4.17)$$

and the third one at $2\omega_m$

$$F_{2\omega} = \frac{1}{4} \frac{\partial C}{\partial z} V_{ac}^2 \cos(2\omega_m t) \quad (4.18)$$

The above equations indicate that the applied AC bias at frequency ω_m is causing the electric force to be modulated at both ω_m and $2\omega_m$. In Eq. 4.17, we notice that when V_{dc} is adjusted to exactly the same as ΔV , F_ω drops to zero; due to the damping, the amplitude of cantilever at frequency ω_m also goes to zero. It is the core idea that “nulling” electric force to measure the local surface potential in AM-KPFM.

In AM-KPFM, the frequency of AC bias is usually, but not necessary, a selected cantilever resonance frequency ω_0 , e.g., $\omega_m = \omega_0$, for enhanced sensitivity afforded by cantilever’s quality factor Q . A potential feedback loop uses amplitude at ω_0 as input and adjusts the feedback signal V_{dc} until the amplitude at ω_0 drops to zero. At this point, V_{dc} equals to CPD between tip and sample; consequently, the 2D local potential mapping is obtained by moving the tip over the sample. In this case, AM-KPFM is done via a dual pass process. The first pass is usually a standard tapping mode or PeakForce tapping (PFT) mode, which measures surface topography. The second pass is KPFM measurement; cantilever is forced to oscillate by an AC bias at cantilever resonance frequency ω_0 . AM-KPFM also can be done via a single pass procedure, which is called “dual-frequency mode.” In dual-frequency mode, an AC bias at frequency ω_m is applied to the tip or sample to null the potential difference between sample and tip, and at the same time, the tapping drive signal at cantilever resonance frequency ω_0 is applied continuously as the tip scans the surface for topographic information. In this case, two different frequencies are involved during imaging process. Usually, the tapping drive frequency is much higher than the surface potential drive frequency, to avoid cross talk of two signals at different frequencies. Dual-frequency mode is more efficient than the dual pass procedure, which saves time and is particularly

suitable for large (>1 V) variations in potential, but the requirement of working far away from cantilever resonance frequency limits the sensitivity of the potential detection. For very small potential variations (<100 mV), the dual pass method is often preferred.

4.4 FM-KPFM

The same as AM-KPFM, in FM-KPFM, an AC bias with frequency ω_m and amplitude V_{ac} , superimposed on a DC bias V_{dc} , is applied between tip and sample [12, 13]. However, the core idea of FM-KPFM is “nulling” the electric force gradient to measure the local surface potential, instead of “nulling” electric force in AM-KPFM. An oscillating electric force gradient, according to Eq. 4.14, is generated between tip and sample, which can be given by

$$\frac{\partial F_e}{\partial z} = -\frac{1}{2} \frac{\partial^2 C}{\partial z^2} \left[V_{dc} - \Delta V + V_{ac} \sin(\omega_m t) \right]^2 \quad (4.19)$$

In the same way, the above equation yields the following three components of the electric force gradient: one at DC

$$\frac{\partial F_{dc}}{\partial z} = -\frac{1}{2} \frac{\partial^2 C}{\partial z^2} \left[(V_{dc} - \Delta V)^2 + \frac{1}{2} V_{ac}^2 \right] \quad (4.20)$$

the second one at ω_m

$$\frac{\partial F_{\omega}}{\partial z} = -\frac{\partial^2 C}{\partial z^2} (V_{dc} - \Delta V) V_{ac} \sin(\omega_m t) \quad (4.21)$$

and the third one at $2\omega_m$

$$\frac{\partial F_{2\omega}}{\partial z} = \frac{1}{4} \frac{\partial^2 C}{\partial z^2} V_{ac}^2 \cos(2\omega_m t). \quad (4.22)$$

We can find in Eq. 4.21 that when V_{dc} is adjusted to exactly the same as ΔV , $\frac{\partial F_{\omega}}{\partial z}$ drops to zero. However, the detection of electric force gradient is not straightforward like amplitude detection. Cantilever resonance frequency shift is usually used to measure electric force gradient.

The fundamental resonance frequency of cantilever ω_0 can be expressed as

$$\omega_0 = \sqrt{\frac{k}{m^*}} \quad (4.23)$$

where k is the spring constant of the cantilever and m^* is the effective mass of the cantilever.

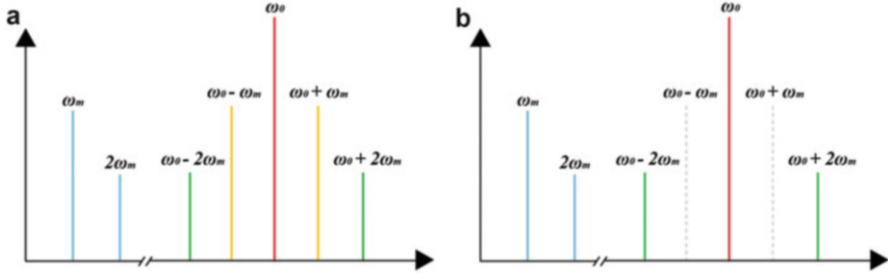


Fig. 4.3 Amplitude versus frequency plot when potential feedback is (a) off and (b) on in FM-KPFM. Applied modulation bias with frequency f_m on cantilever, which is vibrating at its resonance frequency f_0 , modulates the force gradient at both f_m and $2f_m$, leading to side peaks at $f_0 \pm f_m$ and $f_0 \pm 2f_m$. When potential feedback working normally, side peaks at $\omega_0 \pm \omega_m$ will disappear

When a conductive cantilever is oscillating in an electric field, the effective spring constant of the cantilever is changed by electric force gradient; thus

$$k_{eff} = k - \frac{\partial F_e}{\partial z} \quad (4.24)$$

Therefore, for small force gradient (if $\frac{\partial F_e}{\partial z} \ll k$), the resonant frequency shift is

$$\Delta\omega \approx -\frac{\omega_0}{2k} \frac{\partial F_e}{\partial z} \quad (4.25)$$

An AC bias is applied onto a cantilever which is vibrating at its resonance frequency, driving by tapping piezo. The applied AC bias modulates the electric force gradient, which means it also modulates the cantilever resonance frequency. According to Eqs. 4.21 and 4.22, the electrical force gradient is modulated at both AC bias frequency ω_m and the second harmonic $2\omega_m$, so if one mechanically drive the cantilever oscillation at the resonance frequency ω_0 , ω_0 is also modulated at both AC bias frequency ω_m and the second harmonic $2\omega_m$, and it will generate four side peaks at $\omega_0 \pm \omega_m$ and $\omega_0 \pm 2\omega_m$. Figure 4.3a shows the side peaks in FM-KPFM when potential feedback is off and Fig. 4.3b indicates side peaks at $\omega_0 \pm \omega_m$ disappear when potential feedback is on. The amplitude of the side peaks indicates the resonance frequency modulation amplitude. In Eq. 4.21, we notice that when V_{dc} is adjusted to exactly the same as ΔV , the electrical force gradient at ω_m , $\frac{\partial F_e}{\partial z}$, drops to zero. It will result in the amplitude of side peak at $\omega_0 \pm \omega_m$ also going to zero. Using amplitude or phase of side peak at frequency $\omega_0 \pm \omega_m$ as KPFM feedback and adjusting V_{dc} until the side peak disappear is the core idea of “nulling” electric force gradient to measure the local surface potential in FM-KPFM.

Similar with the AM-KPFM, the FM-KPFM also can be done via both single pass and dual pass procedure.

4.5 KPFM Without Potential Feedback

In typical instrument settings, the KPFM measurement covers the potential range up to $\pm 10V$, which is adequate for work function difference measurement. However, for the study of trapped charges on an insulating surface, it is totally a different story. Electrostatic charge may lead to very high voltage; if we still use “nulling” method to measure the voltage difference between tip and sample by Kelvin probe method, a high voltage source must be required. It needs to modify current instruments and is dangerous for operation. An alternative way to realize high voltage measurement in current KPFM instruments is calculation method. In this way, the KPFM potential feedback is turned off, and no additional high voltage source is involved.

The first way for calculating high voltage difference between tip and sample is called “KPFM-HV” mode. According to Eq. 4.17, when KPFM potential feedback is off, e.g., V_{dc} does not change with surface potential change, the electrical force at AC bias frequency ω_m can be expressed as follows:

$$F_\omega = \frac{\partial C}{\partial z} (\Delta V) V_{ac} \sin(\omega_m t) \quad (4.26)$$

The cantilever will be forced oscillated by the driving force F_ω at the modulation frequency ω_m , and the equation for cantilever motion can be written as

$$m^* \frac{d^2 x}{dt^2} = -kx - \gamma m \frac{dx}{dt} + F_\omega \quad (4.27)$$

where x is the position of end of cantilever and γ is the damped coefficient. The solution of Eq. 4.27 is

$$A = \frac{F_0}{m^* \sqrt{(\omega_0^2 - \omega^2)^2 - (\gamma^2 \omega^2)}} \quad (4.28)$$

where A is the amplitude of the cantilever and $F_\omega = F_0 \sin(\omega_m t)$. The above result indicates the amplitude of cantilever is proportional to the driving force. So if we note the amplitude at AC bias frequency ω_m as A_ω , we can get

$$A_\omega \propto \frac{\partial C}{\partial z} (\Delta V) V_{ac} \quad (4.29)$$

The similar process can be used for Eq. 4.18; if we note the amplitude at AC bias second harmonic frequency $2\omega_m$ as $A_{2\omega}$, we can get

$$A_{2\omega} \propto \frac{1}{4} \frac{\partial C}{\partial z} V_{ac}^2 \quad (4.30)$$

If we vibrate the AC bias at a frequency very far away from the cantilever resonance frequency, e.g., both ω_m and $2\omega_m$ are far away from ω_0 , the $A_{2\omega}$ can be considered that it has the same pre-factor as A_ω . So, ΔV can be written as

$$\Delta V = \frac{1}{4} V_{ac} \frac{A_\omega}{A_{2\omega}} \quad (4.31)$$

Using lock-in amplifiers, SPM can measure both A_ω and $A_{2\omega}$; consequently, we can get the potential difference ΔV .

In this method, we can also get $\frac{\partial C}{\partial z}$, which reflects the dielectric constant variations across the sample.

$$\frac{\partial C}{\partial z} = \frac{4A_{2\omega}}{V_{ac}^2} \quad (4.32)$$

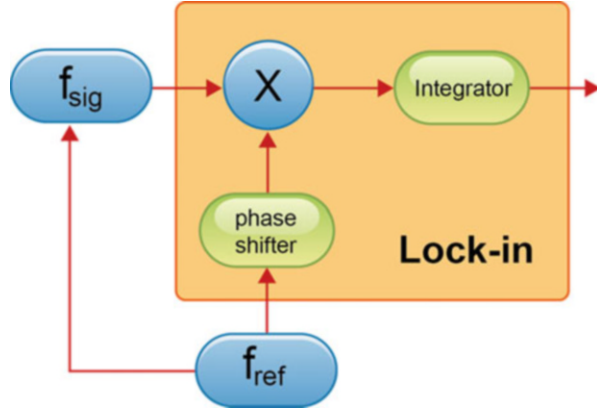
The second way for calculating high voltage difference between tip and sample is extrapolation method. This method only uses the linear relationship between cantilever amplitude A_ω at AC bias frequency ω_m and potential difference between tip and sample $V_{dc} - \Delta V$, according to Eq. 4.17. If we change $V_{dc} - \Delta V$ by applying DC bias on sample or tip, the amplitude A_ω will also change with it linearly. If we plot A_ω versus V_{dc} , A_ω will drop to zero when $\Delta V = V_{dc}$, and at this point, the applied bias V_{dc} nulls the original potential difference between tip and sample. In this case, the idea is exactly the same as AM-KPFM, and we will get a fold line in A_ω versus V_{dc} relationship. However, in the voltage operating range -10 V to $+10$ V, this will not always happen. If the potential difference between tip and sample is larger than ± 10 V and the potential difference between tip and sample cannot be nulled, we will get a straight line in A_ω versus V_{dc} relationship. If we extrapolate the line intersect at $A_\omega = 0$, the value of V_{dc} at the crossover point equals to ΔV .

5 KPFM Measurement

5.1 Lock-In Settings for KPFM Measurement

In current SPM equipment, lock-in amplifiers are very important for KPFM measurement. Lock-in amplifier is a phase-sensitive detector, which can extract a signal with known frequency from an extremely noisy background. It can be understood as a mixer followed by an integrator. The two signals with frequencies f_{ref} and f_{sig} get multiplied in the mixer. If $f_{\text{ref}} = f_{\text{sig}}$, the output of the mixer is a DC voltage with a magnitude proportional to the amplitudes of f_{ref} and f_{sig} ; if $f_{\text{ref}} \neq f_{\text{sig}}$, the output signals of the mixer are with two frequencies $f_{\text{ref}} - f_{\text{sig}}$ and $f_{\text{ref}} + f_{\text{sig}}$. An integration with a long time constant suppresses the new frequencies and the output is zero. In other words, lock-in amplifier can pick up amplitude and phase signal at certain frequency f_{ref} . Figure 4.4 is the schematic diagram of the lock-in amplifier.

Fig. 4.4 Schematic diagram of a lock-in amplifier



In AM-KPFM, a single lock-in is used to read the amplitude and phase at AC bias frequency ω_m for KPFM measurement. The reference frequency f_{ref} of lock-in is set to AC bias frequency ω_m ; consequently, the cantilever oscillation at frequency ω_m can be detected by the lock-in. Signals at other frequencies, such as deflection at DC, which is indicated by Eq. 4.16, and cantilever oscillation at second harmonic $2\omega_m$, which is indicated by Eq. 4.18, are averaged to zero. A potential feedback loop uses cantilever amplitude at ω_m as lock-in input and adjusts the feedback signal V_{dc} until the amplitude at ω_m drops to zero. Figure 4.5 illustrates the AM-KPFM method. However, cantilever amplitude at ω_m is not enough for lock-in to adjust the feedback signal V_{dc} . According to Eq. 4.15, the relationship between electrical force F_e and total potential difference V ($V = V_{dc} - \Delta V + V_{ac} \sin(\omega_m t)$) is not a monotonic function. It means F_e may have the same value when the potential difference V between tip and sample is negative or positive. On the negative side, when V increases, the electrical force F_e will decrease, e.g., F_e is out of phase with V_{ac} ; on the positive side, when V increases, the electrical force F_e will also increase, e.g., F_e is in phase with V_{ac} . So, the cantilever oscillation will have a different phase, relative to the reference signal V_{ac} , depending on whether the tip voltage is larger or smaller than the sample voltage. Both the cantilever amplitude and phase are needed for the feedback loop to correctly adjust V_{dc} . In fact, the input signal to the potential feedback loop is the cantilever amplitude multiplied by the sine of its phase. It means we have to adjust lock-in phase to get correct feedback direction. In the full range of lock-in phase $\pm 180^\circ$, there is a half range which can lead to correct feedback direction and a half range which can result in wrong feedback direction.

In FM-KPFM, the situation is a little complex. It usually uses two cascaded lock-in amplifiers for KPFM measurement, which is shown in Fig. 4.6.

To understand the lock-in setup, we should understand the signal that comes into lock-ins first. According to Eqs. 4.21 and 4.25, the electrical force gradient change at AC bias frequency ω_m will lead to frequency shift $\Delta\omega$

$$\Delta\omega \approx -\frac{\omega_0}{2k} \frac{\partial F_\omega}{\partial z} = \frac{\omega_0}{2k} \frac{\partial^2 C}{\partial z^2} (V_{dc} - \Delta V) V_{ac} \sin(\omega_m t) \quad (4.33)$$

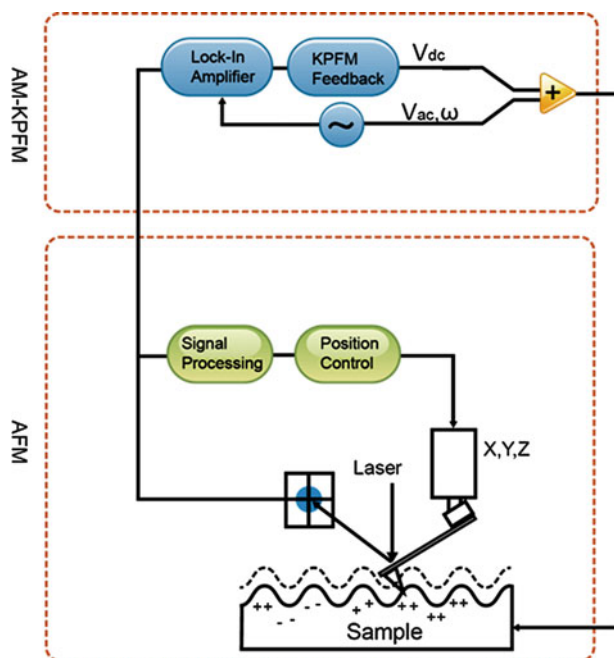


Fig. 4.5 Schematic diagram of AM-KPFM

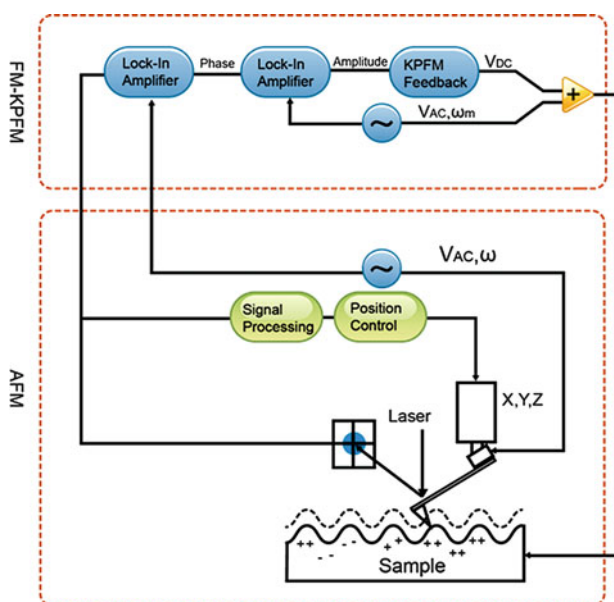


Fig. 4.6 Schematic diagram of FM-KPFM

To simplify the analysis, we note the frequency-modulated amplitude as δf

$$\delta f = \frac{\omega_0}{2k} \frac{\partial^2 C}{\partial z^2} (V_{dc} - \Delta V) V_{ac} \quad (4.34)$$

In FM-KPFM, the cantilever is oscillated at its resonance frequency ω_0 ; if AC bias modulates the frequency at ω_m , the cantilever motion can be written as

$$x(t) = A \sin \left\{ \int_0^t [\omega_0 + \delta f \sin(\omega_m \tau)] d\tau \right\} = A \sin \left[\omega_0 t - \frac{\delta f}{\omega_m} \cos(\omega_m t) \right] \quad (4.35)$$

where A is the amplitude of cantilever. $\delta f \ll \omega_m$ if the above equation can be recast as the following form:

$$x(t) = A \sin(\omega_0 t) - A \frac{\delta f}{\omega_m} \sin(\omega_m t) \cos(\omega_0 t) \quad (4.36)$$

After further transformation, we can get

$$x(t) = A \sin(\omega_0 t) + \frac{A}{2} \frac{\delta f}{\omega_m} \sin[(\omega_0 - \omega_m)t] - \frac{A}{2} \frac{\delta f}{\omega_m} \sin[(\omega_0 + \omega_m)t] \quad (4.37)$$

The above equation indicates that under frequency modulation conditions, cantilever will oscillate at three different frequencies (if $\delta f \ll \omega_m$), e.g., cantilever resonance frequency ω_0 and modulated frequencies $\omega_0 \pm \omega_m$. Using Eq. 4.37, we can easily understand the two side peaks with frequencies at $\omega_0 \pm \omega_m$. Here we only deal with force gradient at ω_m . In real situation, higher-order side peaks $\omega_0 \pm n\omega_m$ will appear.

The cantilever motion signal $x(t)$ goes into the first lock-in amplifier, which reference frequency f_{ref} equals to the cantilever resonance frequency ω_0 . Because the amplitude of the side peaks is hard to be detected directly, the phase output at cantilever resonance frequency will be fed into the second lock-in amplifier for further demodulation. From Eq. 4.36, we know the phase signal can be expressed as

$$\varnothing = \arctan \left(-\frac{\delta f}{\omega_m} \sin(\omega_m t) \right) \quad (4.38)$$

For small angle approximation (if $\delta f \ll \omega_m$),

$$\varnothing = -\frac{\delta f}{\omega_m} \sin(\omega_m t) \quad (4.39)$$

The reference frequency of the second lock-in amplifier is set to AC bias modulation frequency ω_m ; thus the amplitude output of the second lock-in amplifier

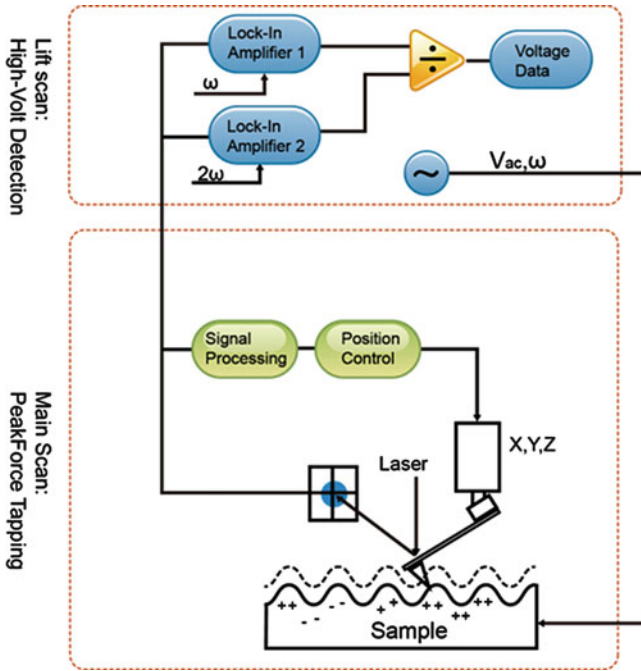


Fig. 4.7 Schematic diagram of KPFM-HV mode

is proportional to $\frac{\delta f}{\omega_m}$, which is also proportional to the amplitude sum of side peaks at $\omega_0 \pm \omega_m$. This signal is then used for KPFM feedback. System adjusts V_{dc} until $\frac{\delta f}{\omega_m}$ drops to zero; at this point, the V_{dc} equals to the potential difference of tip and sample.

In KPFM-HV mode, the potential feedback is turned off, and we use the amplitude of cantilever at AC bias frequency ω_m and the second harmonic $2\omega_m$ to calculate the potential difference. The cantilever motion signal is sent to two separate lock-in amplifiers simultaneously. Reference frequency of one lock-in amplifier is set to AC bias frequency ω_m to detect cantilever amplitude and phase at drive frequency, and reference frequency of the other lock-in amplifier is set to $2\omega_m$ to detect cantilever amplitude and phase at second harmonic. Calculation is done in background to get the potential difference ΔV and $\frac{\partial C}{\partial z}$. The lock-in setting of KPFM-HV mode is shown in Fig. 4.7.

5.2 KPFM Resolution

Let us consider a metal sphere with radius R above an infinite metal plate, the separation is Z . This model is shown in Fig. 4.8. The metal sphere serves as KPFM probe and the infinite metal plate serves as KPFM sample.

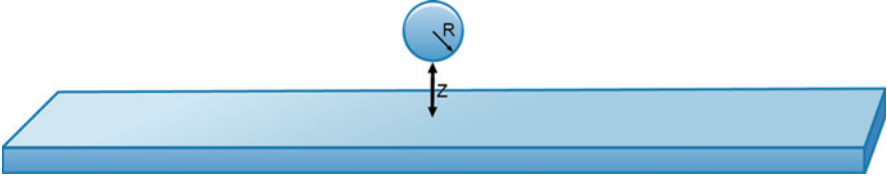


Fig. 4.8 A simple model to study KPFM spatial resolution

If the potential difference between the sphere and the part of plate just below is ΔV , the electrical force between the two objects can be written as

$$F(z) = -\pi\epsilon_0 \left[\frac{R^2}{z(z+R)} \right] \Delta V^2 \quad (4.40)$$

And the electrical force gradient is

$$\frac{\partial F}{\partial z} = -\pi\epsilon_0 \left(\frac{1}{z} + \frac{1}{z+R} \right) \left[\frac{R^2}{z(z+R)} \right] \Delta V^2 \quad (4.41)$$

For AM-KPFM, the spatial resolution depends on the relationship between $F(z)$ and z , and for FM-KPFM, the spatial resolution depends on the relationship between $\frac{\partial F}{\partial z}$ and z . Obviously, the electric force gradient has a steeper dependence on Z than the electric force. It also has a steeper dependence on X and Y . It is the reason why FM-KPFM has better resolution than AM-KPFM.

Some experiments were done to study KPFM spatial resolution [13]. The result shows FM-KPFM has higher resolution than AM-KPFM, because larger than half of the FM-KPFM signal is contributed by the foremost 0.3 % of the tip cone; but for AM-KPFM, the contribution from the tip cone never reaches 50 %. It indicates the lateral resolution of FM-KPFM can achieve about 50 nm but AM-KPFM often several micrometers.

So in KPFM, the measured potential in KPFM is actually an average of the sample potential, especially in AM-KPFM. The convolution always happens. The measurements of the potential will be distorted due to the nonuniform capacitive coupling between the tip and various parts of the surface. The measured potential by KPFM is not the real local potential, but a weighted potential. The substrate can be modeled as n electrodes of constant potential V_i , and the relationship between measured potential and real local potential can be expressed as [14]

$$V_{dc} = \frac{\sum_{i=1}^n \left(\frac{\partial C_{it}}{\partial z} V_i \right)}{\sum_{i=1}^n \left(\frac{\partial C_{it}}{\partial z} \right)} \quad (4.42)$$

where V_{dc} is the measured potential, V_i is the local surface potential at point i on the substrate, and $\frac{\partial C_{it}}{\partial z}$ is the change rate of the capacitance with respect to the distance

between the tip and point i on the substrate. The weighting factors are the derivatives in z of tip–surface capacitances, which can be defined as follows:

$$h_i = \frac{\frac{\partial C_{it}}{\partial z}}{\sum_{i=1}^n \left(\frac{\partial C_{it}}{\partial z} \right)} \quad (4.43)$$

Although the potential is averaged, the total charge still can be calculated by the potential image.

5.3 KPFM Sensitivity

Usually the FM-KPFM has less sensitivity in air than AM-KPFM, and this is a major reason why FM-KPFM is usually performed in vacuum. However, the sensitivity of FM-KPFM can be improved if we know the factors which affect its sensitivity. According to Eq. 4.25, the frequency shift induced by force gradient is proportional to the cantilever resonance frequency ω_0 and inversely proportional to the cantilever spring constant k . Consider the cantilever as a simple harmonic oscillator; near its resonance frequency, if frequency changes $\frac{\omega_0}{Q}$, the phase will change $\frac{\pi}{2}$. Consequently, if frequency shifts $\Delta\omega$, the phase shift can be written as

$$\Delta\varphi = \frac{\frac{\pi}{2} \Delta\omega}{\frac{\omega_0}{Q}} = -\frac{\pi}{4} \frac{Q}{k} \frac{\partial F_e}{\partial z} \quad (4.44)$$

So the FM-KPFM sensitivity is proportional to $\frac{Q}{k}$. This result also applies to AM-KPFM. However, it is of particular significance to FM-KPFM, which has lower signal as only the front part of the tip contributes. For AM-KPFM in air, the KPFM signal comes from not only the tip but also cantilever. The signal is usually large enough to get sufficient sensitivity.

From another viewpoint, the force gradient can be considered as an additional spring constant. If cantilever nature spring constant k is small, the same force gradient will lead to relative large change of it, so smaller spring constant indicates higher sensitivity. Furthermore, if the quality factor Q is large, the phase versus frequency plots steeper, and around the cantilever resonance frequency, phase change directly reflects frequency shift (almost linear), so large quality factor also indicates higher sensitivity.

For FM-KPFM, to improve its sensitive, we can increase Q or decrease k . Putting the system into a vacuum environment can dramatically increase Q factor; thus sufficient sensitivity can be achieved. Using probes with large Q and small k also can improve FM-KPFM sensitivity, but for tapping mode, Q cannot be very large and k cannot be very small; for PeakForce tapping,

this limitation is gone, so PeakForce KPFM can work very well in air with high sensitivity.

5.4 KPFM Repeatability

There are several factors that can affect KPFM repeatability. The major reason is the work function of the probe. If the work function of the probe is different from each other, the experiment results are different. Probe made by single materials with unique work function is vital for KPFM repeatability.

Another factor which can affect the KPFM repeatability is the separation between tip and sample. This separation includes the lift height and cantilever amplitude.

Besides above, sometimes there is current flow between tip and sample, which can lead to electrochemical reactions. This factor also makes surface potential change.

Sample or probe surface oxidation, adsorption of molecules, and so on will also result in bad KPFM repeatability.

6 Applications of KPFM in Nanoscale Characterization

Based on the above discussion, KPFM plays an important role in material electrical property mapping. In this section, we will discuss the applications of KPFM in characterization of inorganic nanostructure and nanomaterials. We will mainly focus on five KPFM applications including surface charge detection, work function and doping level study, charge transfer study, FETs, and atomic resolution KPFM.

6.1 Surface Charge

By measuring the surface potential of the sample with KPFM, the electric quantity can be obtained. A quantitative method was developed to count the electric quantity formed when an AFM tip rubs against a SiO_2/Si substrate [9]. The measured potential by KPFM is not the real local potential, but a weighted potential. By using Eqs. 4.43 and 4.44 mentioned above, the real surface potential can be obtained by summing up the measured potential V_{DC} at each point. The capacitance is calculated to be 8.96×10^{-18} F. The electric quantity formed in contact and friction process can be estimated by converting the surface potential from the system capacitance.

Then, the nanotriboelectrification between the tip and the substrate can be investigated quantitatively [9]. As shown in Fig. 4.9b–e, the loaded force between the tip and substrate caused the charge sign reversal, i.e., when applying large loaded force, positive charge formed in the friction or contact areas, and when

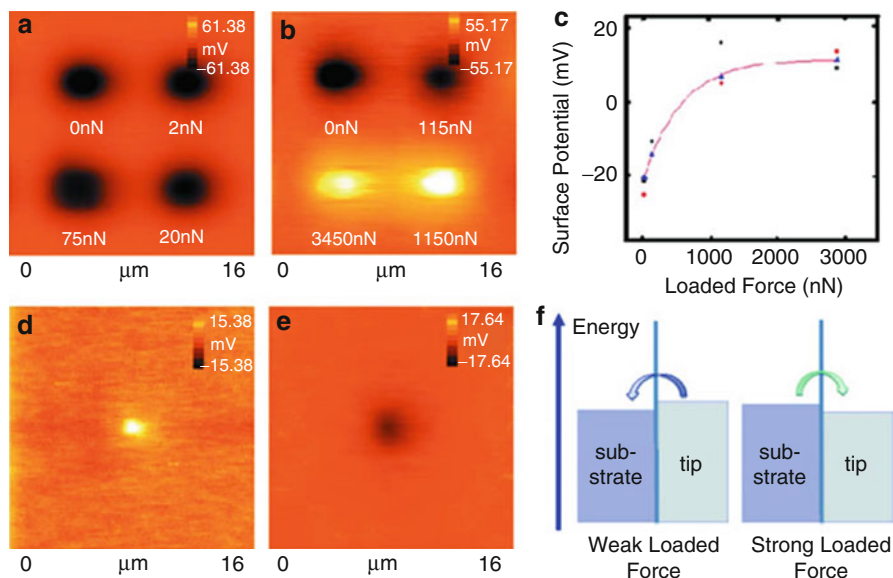


Fig. 4.9 (a) and (b) The potential images obtained by using different tips on SiO_x substrates. The corresponding loaded forces are shown under each charge pattern. (c) The loaded force dependence of surface potential when scanning over the SiO_x surface. (d) and (e) The potential images of contact experiments obtained by applying different loaded forces. (d) 3,450 nN and (e) 115 nN. (f) The scheme of charge sign reversal model. The *arrow* shows the direction of the electron flow (Reprinted with permission from [9]. Copyright (2010), AIP Publishing LLC)

applying small loaded force, negative charge formed in the friction or contact areas. This charge reversal was attributed to the pressure-induced surface state change.

Nanotriboelectrification can be used to realize high-speed dip-pen nanolithography (DPN) [15]. As stated above, KPFM measurements show the region on the substrate where the AFM tip rubbed was charged. Then, the electrostatic interaction resulting from the charge can be employed to fabricate nanopatterns. The nanoparticles loaded on the tip were transported onto the substrate as the AFM tip moved at a speed as high as hundreds of $\mu\text{m/s}$. The so-called nanoxerography [16–19] has emerged as a versatile method for assembling nanoparticles from solution onto solid templates. It uses the strong electric fields generated by charge patterns written onto substrate to trap charged or polarizable nanomaterials via electrostatic interactions.

KPFM has also been used to investigate charging and discharging of graphene sheets [20, 21]. Charge can transfer between reduced graphene oxide (rGO) sheets separated in hundreds of nanometers on insulating substrates [20]. Figure 4.10a shows a selected rGO sheet on SiO₂ surface which was cut into four pieces (labeled with 4, 5, 6, and 7, respectively) by an AFM tip. The separation distances between the rGO-4 and rGO-5, rGO-5, and rGO-6, and rGO-6, and rGO-7 are 150, 150, and 300 nm, respectively, while the corresponding gap lengths are 2,000 nm, 650 nm, and 2,000 nm, respectively. After rGO-4 is charged by an AFM tip bias, KPFM image (Fig. 4.10b)

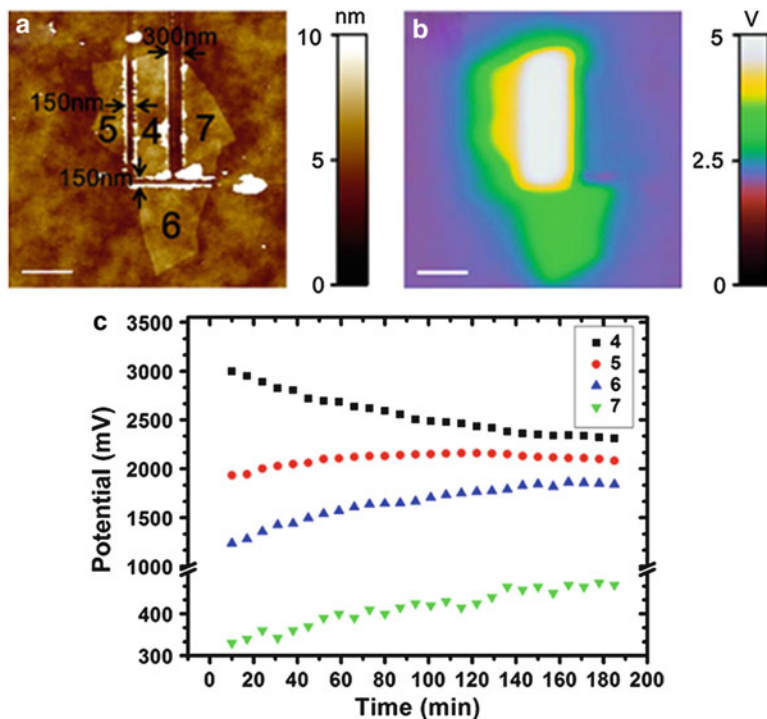


Fig. 4.10 (a) Topological image of an rGO sheet that was cut into four separated pieces on SiO₂. The four rGO sheets were indicated with number 4–7, respectively. (b) KPFM image taken after the rGO-4 was charged with an AFM tip biased at 12 V for 5 min. (c) The time evolution of the surface potentials of the rGO sheets shown in (a) and (b) (Reprinted with permission from [20]. Copyright (2013), AIP Publishing LLC)

revealed that rGO sheets 4–7 had surface potentials of 3.04, 1.93, 1.24, and 0.33 V, respectively. Obviously, the charges transferring from the rGO-4 to rGO-6 were less than to the rGO-5 due to the smaller gap length, while charges transferring from the rGO-4 to rGO-7 were less than to the rGO-5 due to larger separation. The surface potential of rGO-4 decreased from 3,000 mV to 2,300 mV in 180 min, implying that the charges transferred to its surroundings, so the surface potentials of rGO-5, rGO-6, and rGO-7 increased. This automatic discharging and charging is very slow in a time scale of hours (Fig. 4.10c). When the surface potentials reached equilibrium after about 3 h, there were still distinct differences between their values, reflecting approximately the threshold potential that limited further charge transfer. Apparently, threshold potential increases along with the increase of the separation distance and decrease of the gap length between the rGO sheets.

Humidity in ambient conditions can affect the discharging process [21]. The time evolution of KPFM images of a few-layered graphene (FLG) film indicates the main discharge process is through water molecules adsorbed on the FLG film itself and the water film on the SiO₂ substrate [22]. In fact, water adsorption layers play a

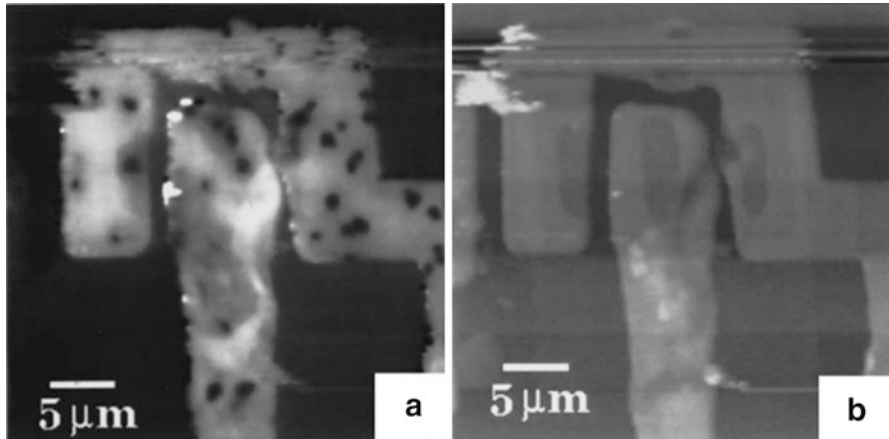


Fig. 4.11 (a) KPFM image of Al/Cu film showing contrast between Al and the Al/Cu intermetallic (Al_2Cu). (b) AFM topography image of the Al/Cu film in (a), recorded simultaneously with the KPFM image (Reprinted with permission from [6]. Copyright (1999), AIP Publishing LLC)

very important role in KPFM measurements [23]. It was found that the thickness of water adsorption layer on the metal surfaces of chromium, copper, and gold increases with the rise of humidity. The surface potential measured by KPFM decreases with the increasing humidity due to water adsorption on the metal. And the reduction of surface potential with the rise of relative humidity is different for these three samples, resulting from the different thickness of adsorbed water layer on their surfaces, which is determined by the different surface properties, such as the roughness and contact angle.

6.2 Work Function and Doping Level

6.2.1 Metallic Nanostructures

KPFM was first developed to investigate contact potential difference (CPD) between metallic materials including gold, platinum, and palladium surfaces [5]. The CPD between two materials depends on a variety of parameters such as the work function, adsorption layers, oxide layers, dopant concentration in semiconductors, or temperature changes on the sample [5, 24].

KPFM is capable of distinguishing different intermetallics in a metal alloy due to the different work functions [6]. As shown in Fig. 4.11b, the topographic image shows the regular topography of the lines with no other contrast. However, the corresponding CPD image (Fig. 4.11a) shows strong contrast that dark patches are observed within the bright background. These are regions which contain intermetallic compound Al_2Cu , which are known to decorate the grain boundaries. The contact potential difference in these regions was 150 mV lower than that of the surrounding Al regions. The spatial resolution reached in these experiments is around 50 nm and the sensitivity to the CPD measurement was

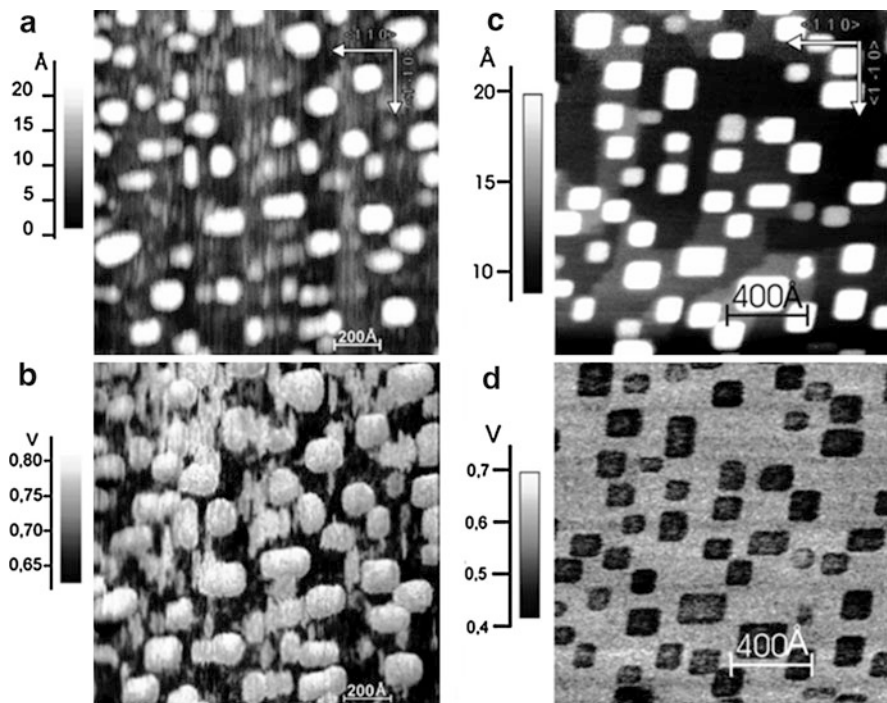


Fig. 4.12 Topography and CPD images of Au nanostructures on InSb (001) surface before and after annealing. Topographical image (a) and corresponding CPD image (b) of Au/InSb (001) system. Topographical image (c) and corresponding CPD image (d) of Au/InSb (001) system after annealing at 650 K for 2 h (Reprinted with permission from [25]. Copyright (2005), AIP Publishing LLC)

approximately 0.12 mV. It is obvious that KPFM is capable of detecting sample work function especially on the nanometer scale [6].

Au nanostructures deposited on InSb (001) surface were carefully studied [25, 26]. Au nanostructures were predominantly to form rectangular islands, and the typical height of the islands corresponds to a few monolayers (MLs) of gold. And it was found that the work function was independent on the size of the Au nanostructure. Figure 4.12a and b shows the topography and corresponding CPD mapping of Au nanostructures [25]. The CPD mapping provides more details than surface topography. As shown in Fig. 4.12b, both the islands and the features between the islands have the same higher work function than the one corresponding to the substrate material. Accordingly, it is known that the work function of pure gold is higher than the one for clean InSb. However, the contrast between the Au nanostructures and InSb substrate is reversed after high temperature annealing (Fig. 4.12d), indicating that the nanostructures assembled after the annealing process have the lower work function than the substrate. This is most likely due to indium alloying with gold to form the nanostructures, which results in the Sb-rich substrate between the islands.

6.2.2 Semiconducting Nanostructures

KPFM has been used to study the quantum effect of nanostructures locally. By comparing the topographic and CPD images of InAs quantum dots (QDs) with the size varying from 1.3 to 7.2 nm, it was found that CPD decreases with increasing height. This dependence is governed by quantum size effects, i. e., the amount of charges accumulated in the QD are determined by the confinement energy levels [7].

Topographic and CPD images of ~ 40 nm InSb nanodots grown on GaAs substrates were measured [27]. Though an obvious correlation between the two images is observed, the dark rings around the dots observed in the CPD image and the CPD peak heights do not match the work function difference between InSb and GaAs, indicating the composition changes. An additional CPD peak on each side outside the dot area is also measured by the KPFM, which is consistent with the estimated CPD signal variations by taking into account the strain and the composition changes within and around individual nanodots.

KPFM is a powerful technique in characterizing two-dimensional (2D) materials such as MoS₂ [28, 29]. For MoS₂ nanoflakes annealed at 350 °C in Ar atmosphere, their Fermi levels can be measured with KPFM as shown in Fig. 4.13 [30]. The Fermi-level shift exhibits exponential decay with the thickness of flakes, indicating the interlayer screening effect exists. The CPD between three layers and two layers was ~ 170 mV, but the CPD does not change much when the thickness varied from 2.5 nm (about three layers) to 8.7 nm (about ten layers), suggesting that the screening length of MoS₂ flakes is about three or four layers. The screening effect is also observed in graphene [8, 31] and graphene oxide [32].

6.2.3 Carbon Nanostructures

Work function of carbon nanotubes (CNTs) was normally measured by ultraviolet photoelectron spectroscopy (UPS) and found to be ~ 4.8 eV [33–35]. In fact, KPFM is also capable to detect work function of CNTs [36]. Different treatment or modification (treated with nitric acid, UV, and X-ray, or decorated with metal nanoparticles) will obviously change the CPD of metallic single-walled carbon nanotube (SWCNT) networks, indicating the change of work function. However, comparing the UPS and KPFM measurements both before and after UV exposure reveals that the work functions from UPS measurements are generally lower than those measured by KPFM. The reason is that KPFM measures the local work function difference over a relative small scan area, whereas UPS measures the lowest work function patch on the surface.

It is known that SWCNT field effect transistors (FETs) show p-type characteristics in air [37, 38] and n-type characteristics in ultra-high vacuum (UHV) or inert gases [39, 40]. KPFM and electrostatic force microscopy (EFM) were used to study the mechanism [41]. As shown in Fig. 4.14b and c, the CPDs between the Au substrate and the adsorbed SWCNTs are about -0.06 V for Au (111) in air, whereas they are 0.05 V for Au (111) in UHV. The CPD measurements indicate that the energy-level alignment at SWCNT/Au interfaces is strongly sensitive to the presence of oxygen, suggesting that the vacuum level of the SWCNT is lower than that

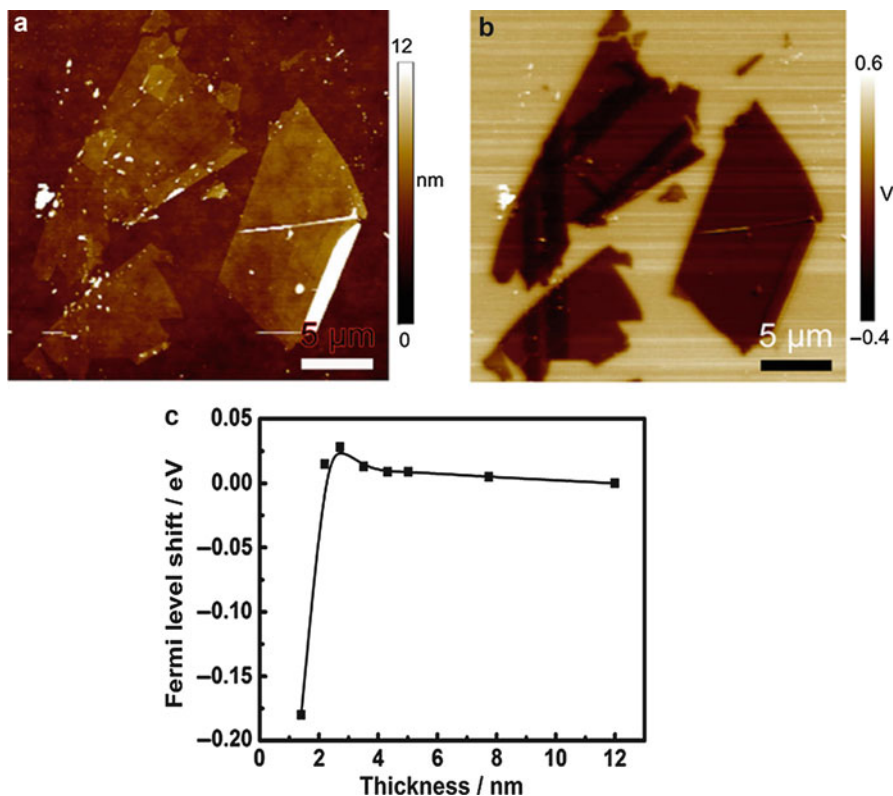


Fig. 4.13 (a) Topography of annealed MoS₂ nanoflakes and (b) corresponding KPFM image of MoS₂ nanoflakes. (c) Fermi-level shift of annealed MoS₂ nanoflakes as a function of thickness (Reprinted with permission from [30]. Copyright (2013), AIP Publishing LLC)

of Au in air but is higher in UHV. EFM measurements show that the interface dipole at the SWCNT/Au interface points from SWCNT (+) to Au (−) in air but reverses its direction in UHV or in a clean N₂ atmosphere. From the EFM measurements, it can be deduced that the SWCNTs on Au are negatively charged with a line density of about 0.1–0.05 e/nm in oxygen-free environments but positively charged with approximately 1 e/nm in air. Therefore, the Au Fermi level lies above the SWCNT mid-gap in vacuum or in inert gases and below the mid-gap in air.

The work function of graphene can also be studied by KPFM. For epitaxial graphene grown on 6H-SiC (0001), KPFM was used to distinguish graphene layers from substrate [42]. As shown in Fig. 4.15a, carbon-rich interface layer (IFL) of SiC substrate, single-layer graphene (1LG), and bilayer graphene (2LG) regions were measured. These regions are hardly visible in the topography image due to coincidence with a compensating step of the SiC substrate; however, the work function difference between 1LG and 2LG is 135 ± 9 meV. Bilayer films are found to have the higher work function than single-layer films due to the doping-induced shift of Fermi level. This method allows an unambiguous distinction between IFL, 1LG,

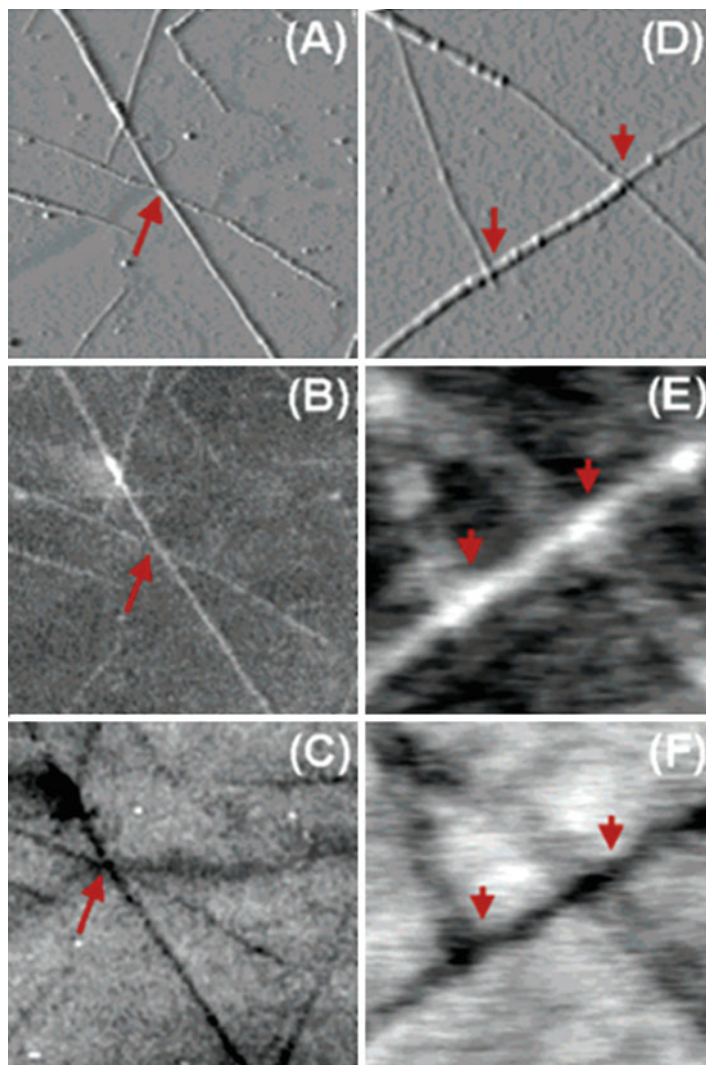


Fig. 4.14 AFM, KPFM, and EFM images of SWCNTs on Au (111) substrates in controlled environments. (a, d) Topographic images of nanotubes deposited on flame-annealed Au surfaces. (b, c) KPFM images obtained in air and after a long period in UHV, respectively. (e, f) EFM images taken in air and in an ambient N_2 environment, respectively (Reprinted with permission from [41]. Copyright (2003) American Chemical Society)

and 2LG. In combination with high-resolution topographic imaging (Fig. 4.15d, e), the complex step structure of epitaxial graphene can be resolved with respect to substrate and graphene layer steps.

Graphene samples can be p-doped when depositing on SiO_2 substrates [43]. KPFM is able to evaluate the doping level [8]. As shown in Fig. 4.16d, the

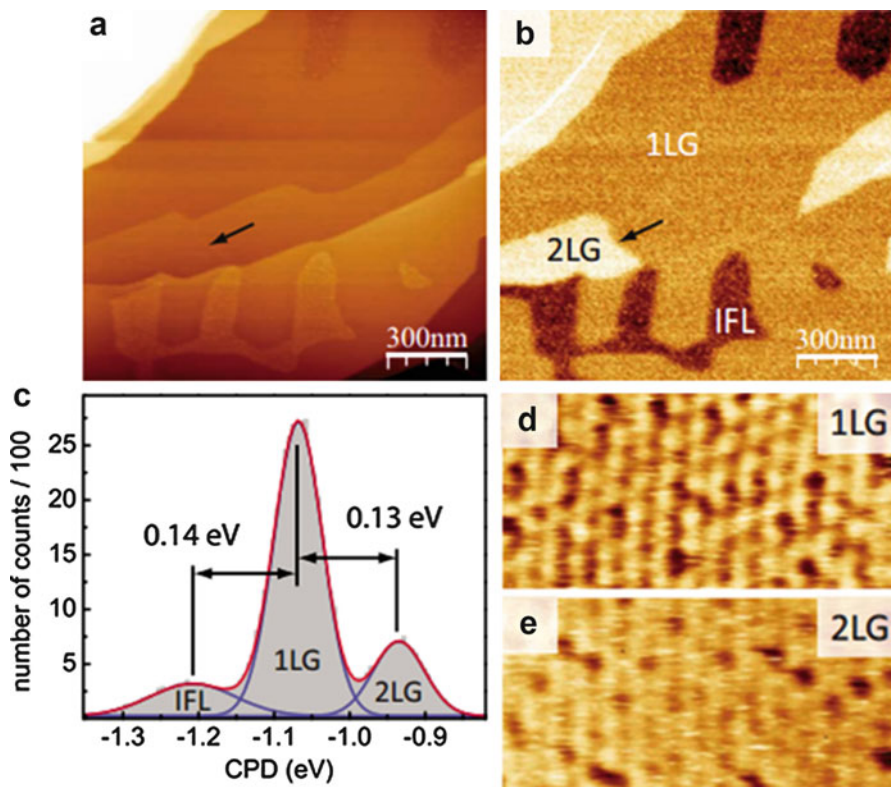


Fig. 4.15 (a) Topography image of a graphene film epitaxially grown on SiC (0001). (b) CPD map identifying the IFL, 1LG, and 2LG. The *arrows* in (a) and (b) indicate the position of a boundary between single and bilayer regions of graphene. (c) Histogram of the CPD map. (d) and (e) High-resolution topography images of single and bilayer films, respectively (Reprinted with permission from [42]. Copyright (2008), AIP Publishing LLC)

surface potential difference between the 1LG and 2LG region is ~ 68 meV. The KPFM measurements revealed significant work function variations as a function of the number of graphene layers, in quantitative agreement with *ab initio* density functional theory (DFT)-calculated work functions for substrate-induced p-doped multilayer graphene (Fig. 4.16g). Work function variation between 1LG and 2LG is mainly due to the shift of the Fermi energy, while for more than two layers, the interlayer screening effects begin to stand out [31]. Raman G band frequency is a function of doping level n [44, 45]. Combining with the Raman data shown in Fig. 4.16g, 1LG has the hole doping level of $n \approx -(2.5 \pm 1) \times 10^{12} \text{ cm}^{-2}$ and 2LG $n \approx -(7.5 \pm 1.5) \times 10^{12} \text{ cm}^{-2}$.

As described above, doping level of graphene can be deduced from the work function of graphene, indicating KPFM might be a valid method to evaluate the doping level [46–51].

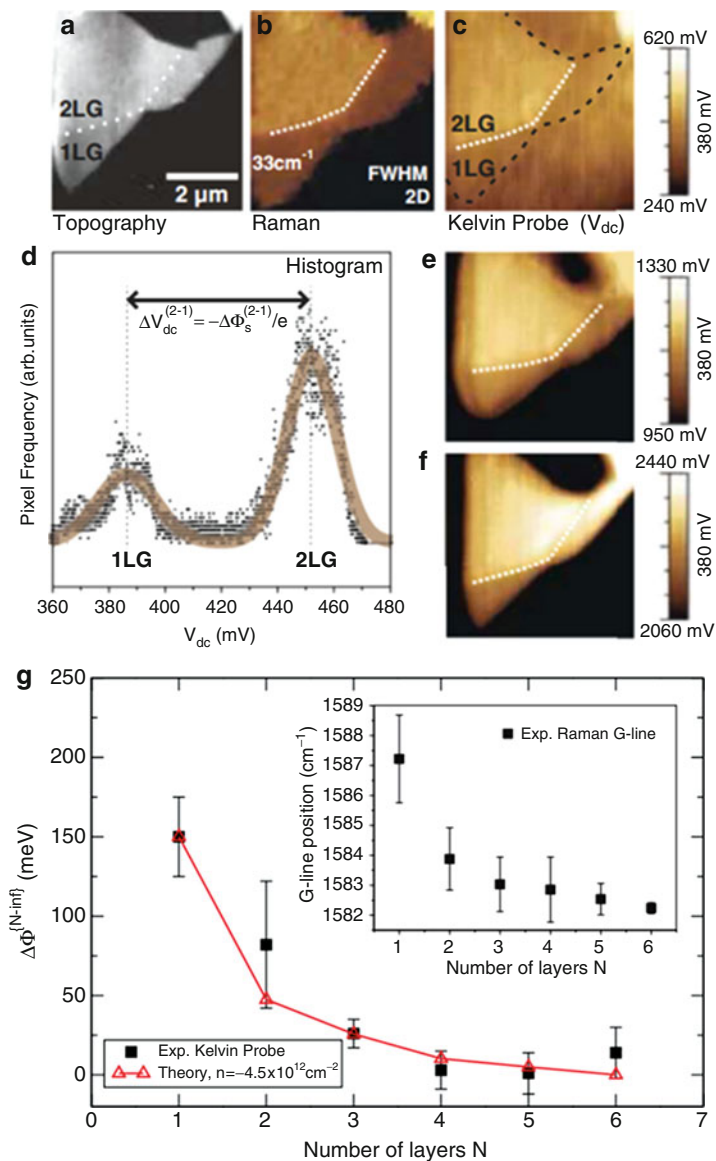


Fig. 4.16 (a) AFM topography image of an isolated graphitic flake consisting of single- and bilayer regions (b) showing the FWHM of the 2D Raman line (c), (e), and (f) surface potential data. (d) Histogram analysis of the acquired surface potential data. The two peaks can be attributed to the 1LG and 2LG regions and a surface potential difference of $\Delta V_{dc}^{(2-1)} \approx 66$ mV is observed. (g) Work function differences as a function of the layer thickness, extracted by histogram analysis of the acquired surface potential data. (*Inset*) Raman G-line shift (Reprinted with permission from [8]. Copyright (2011) by the American Physical Society)

Using the electric field effect, the work function of graphene can be adjusted as the gate voltage tunes the Fermi level across the charge neutrality point, so the intrinsic work function without any doping can be measured by KPFM [11]. The work function of pristine single-layered graphene (SLG) and bilayer graphene (BLG) without any doping is 4.57 ± 0.05 eV and 4.69 ± 0.05 eV, respectively. These values are in reasonable agreement with theoretical estimations [52].

6.3 Charge Transfer

Charge transfer is very important in photovoltaic, electroluminescence, and photocatalysis processes. KPFM is a powerful technique in studying charge transfer in situ.

KPFM can be used to study the interaction between QDs and silicon substrates and the effect of substrate on photoionization. For example, the photoionization of CdSe/CdS core/shell nanocrystals on n- and p-type silicon substrates with 2 nm surface oxide was investigated by KPFM [53]. The measured work function difference between the two substrates is substantially lower (on the order of 300 meV) than flat band degenerately doped n- and p-type silicon (~ 1 eV). This creates upward or downward band bending in the n- and p-type silicon, respectively, and causes Fermi-level pinning at the surface [54]. This band bending influences photoionization by controlling the concentration of photogenerated electrons at the Si/SiO₂ interface, indicating that ultimate control over photoionization is possible.

Platinum-loaded titanium dioxide (TiO₂) is well known for applications in photocatalysis toward water cleavage [55]. The work functions of Pt adatoms [56] and Pt clusters [57] deposited on TiO₂ surface were carefully studied by KPFM. Topographic images identify Pt atoms adsorbed at three different sites: on the Ti atom rows, on the O atom rows, and in O atom vacancies. Most Pt adatoms were observed on Ti atom rows. And successively recorded images show that the Pt adatoms on Ti atom rows (adatoms A) and O atom rows are mobile, while the adatoms in the O atom vacancies (adatoms B) are not. Adatoms A and adatoms B were identified in KPFM images. However, adatoms on O atom rows were not visualized in KPFM images because they moved quickly or were swept out by the tip. Figure 4.17a and b shows a simultaneously recorded topography image and a work function map of the Pt-evaporated surface, respectively. In the topographic image, both the adatoms and O atom rows are resolved. The positions of the Pt adatoms are darker than the surrounding TiO₂ surface, indicating a work function decrease on the Pt adatoms. Figure 4.17e shows that the most probable work function decrease lies in the section between 0.24 and 0.26 eV. The distribution for adatoms B is centered at a larger work function decrease, between 0.26 and 0.28 eV. The work function of Pt on Ti atom row is larger than that on the O atom row by 0.02 eV. The work function of the Pt adatoms is always smaller than that of surrounding TiO₂ surface, indicating that the electron transfer from the adatoms to the surface was induced by an electric dipole moment directed from the substrate to

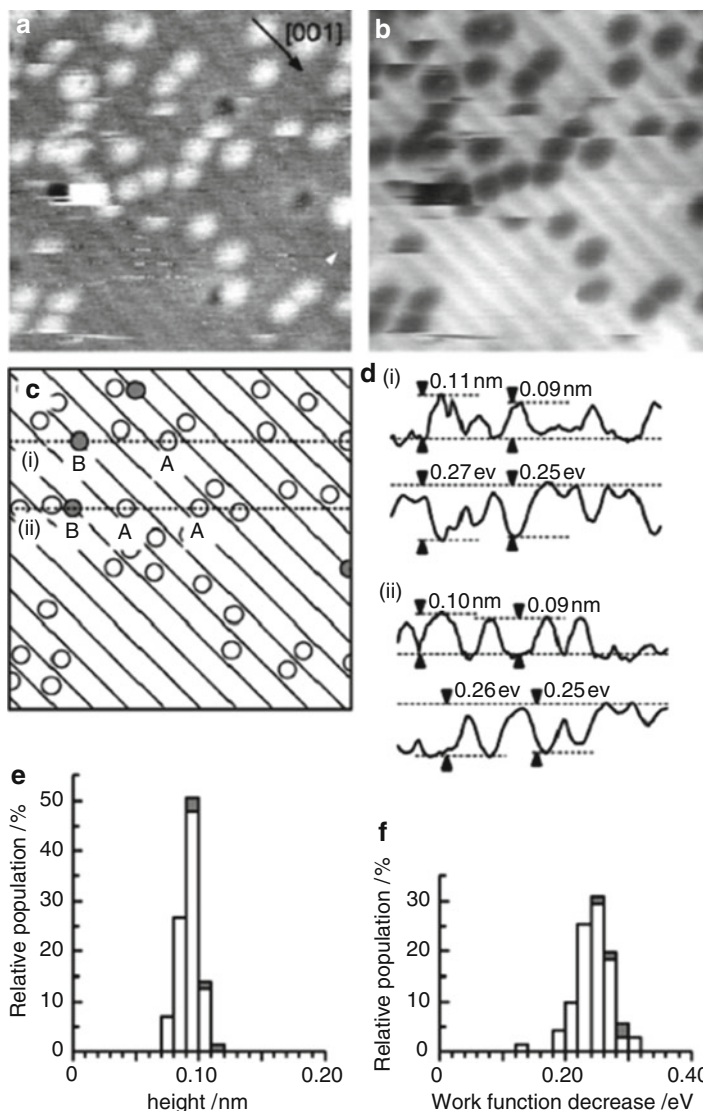


Fig. 4.17 Simultaneously obtained (a) topography and (b) work function map of the Pt-evaporated TiO₂ surface. (c) Model of the surface in (a). (d) Cross sections along the lines in (c). Distribution of the (e) heights from the O atom rows and (f) work function decrease on the Pt adatoms (Reprinted with permission from [56]. Copyright (2006) American Chemical Society)

the vacuum. The difference in work function decrease between adatoms A and B is presumably due to the number of Ti atoms which receive the electrons. Electrons from adatoms A are received by one Ti atom which is originally coordinated to five O atoms. However, it is geometrically possible for an adatom B to have two neighboring Ti atoms, which may enhance the electron transfer.

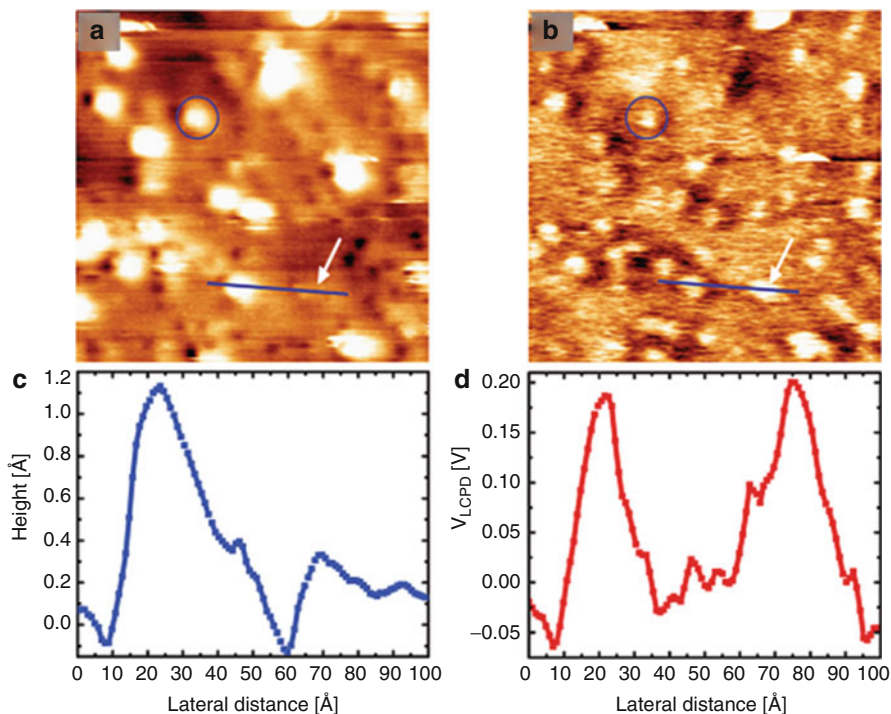


Fig. 4.18 (a) Topography and (b) KPFM image of the Au adsorbed hydroxylated TiO_2 (110) surface. (c) Height and (d) CPD profiles are taken along the line drawn in (a) and (b), respectively. The circle indicates the Au nanocluster (Reprinted with permission from [59]. Copyright (2011), AIP Publishing LLC)

Similar observation of lower work function of Pt than TiO_2 support was found in the system of Pt cluster on TiO_2 [57]. And the work function on the clusters decreases as the interface area increases no matter the clusters were on terraces or at step edges. This might be caused by the electric dipoles formed at the interface of Pt cluster and TiO_2 .

Rutile TiO_2 (110)-(1×1)-supported gold (Au) nanoclusters have been anticipated to fulfill their potential in catalysis and sensor applications, particularly due to the unique size-dependent characteristics of Au clusters and the photocatalytic properties of the supporting TiO_2 surface [58]. Hydroxylated TiO_2 (110) supported Au nanoclusters was carefully studied using KPFM [59]. Figure 4.18a and b shows Au nanoclusters evaporated on TiO_2 surface. The KPFM image in Fig. 4.18b exhibits an increase in the CPD contrast of the surface over the Au nanoclusters compared to the supporting TiO_2 surface. Some atomic species in faint contrast in the topographical image (highlighted by an arrow) are also clearly visible in the CPD image. Figure 4.18d shows Au nanocluster has an average CPD of ~ 200 mV higher than the TiO_2 substrate. Similarly to Pt/ TiO_2 system described above, it was believed that the main contribution to the observed CPD shift over the Au clusters

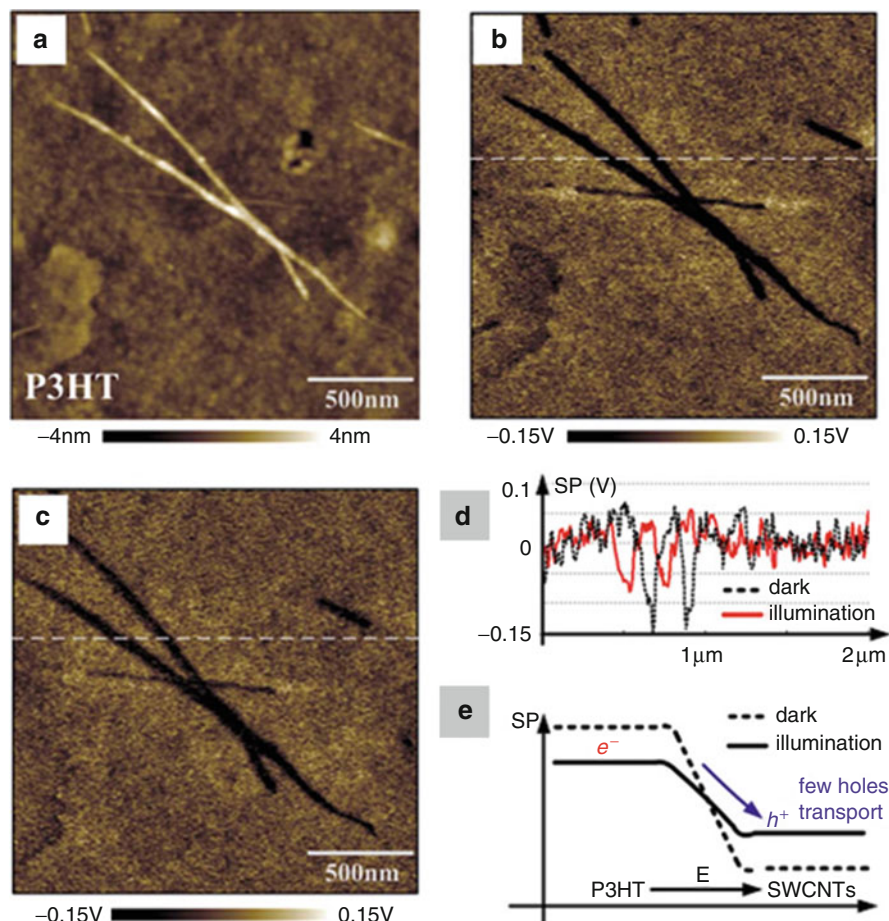


Fig. 4.19 (a) Topography of SWCNTs on *top* of P3HT in the dark. (b) KPFM image in the dark. (c) KPFM image under illumination. (d) Surface potential values of the cross section indicated by the *dash line* in KPFM images. (e) Schematic to show the charge transport (Reprinted with permission from [10]. Copyright (2010), AIP Publishing LLC)

originated from the electric dipole formed between an Au nanocluster and the TiO_2 interface induced by the Au– TiO_2 charge transfer.

Organic solar cells (OSCs) have drawn much attention because of the low cost and high-throughput solution processes [60–62]. It was reported that introducing carbon nanotubes into active layer of OSCs improves the power conversion efficiency [63, 64] and possesses high open-circuit voltage [65, 66]. Photoinduced holes transported from active layer to SWCNTs was observed using KPFM when SWCNTs fabricated on poly(3-hexylthiophene) (P3HT) film as well as on P3HT and 6,6-phenyl-C61-butyric acid methyl ester (PCBM) blended film [10, 67]. SWCNTs were carefully coated on top of P3HT in order to expose both P3HT and SWCNTs (Fig. 4.19a). Compared with Fig. 4.19b (obtained in the dark)

and c (obtained under illumination), surface potential contrast between SWCNTs and P3HT slightly decreased from 0.14 V in the dark to 0.08 V under illumination, indicating the transport of photoexcited carriers from active layer (P3HT) to SWCNTs, which is illustrated in Fig. 4.19e. In the dark, surface potential of P3HT is higher than that of SWCNTs, suggesting the direction of local electric field is from P3HT to SWCNTs. After light absorption by P3HT, photoexcited holes are driven to SWCNTs by the local electric field at the interface between P3HT and SWCNTs while electrons tend to remain in P3HT. The reduced surface potential contrast under illumination is attributed to the induced electric field by photoexcited electrons in P3HT and holes in SWCNTs, which has opposite direction as the local electric field in the dark. Compared with SWCNTs on P3HT, decrease of surface potential contrast between SWCNTs and P3HT/PCBM under illumination is more significant, indicating more holes transport from active layer P3HT/PCBM to SWCNTs. KPFM study on P3HT/PCBM/SWCNTs demonstrates that photoinduced holes are present in SWCNTs and thus SWCNTs work as donor, which is coincident with the macroscopic fact that introducing SWCNTs in P3HT/PCBM solar cells can increase the power conversion efficiency.

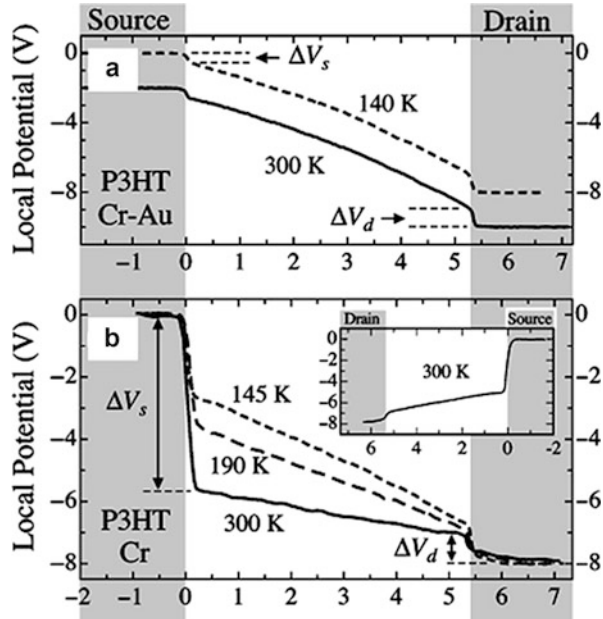
6.4 Field Effect Transistors

Experimental techniques providing valuable electrical, mechanical, and processing properties are critical to the development of FETs. KPFM provides a two-dimensional profile of surface potentials, ideal for characterizing transistor structures.

The performance of thin-film field effect transistors (TFTs) based on conjugated organic materials as the active semiconducting component has experienced impressive improvement in recent years [68]. Bottom-contact polymer FETs made from P3HT were studied by KPFM [69]. Figure 4.20 shows the abrupt voltage drops ΔV_s and ΔV_d caused by source and drain contact resistance, respectively. As illustrated in Fig. 4.20a, very small contact voltage losses occurred, suggesting Cr–Au electrodes form a relatively good contact for P3HT. However, ΔV_s and ΔV_d , and therefore the source and drain contact resistance, are nearly equal in the case of P3HT/Cr–Au. For FETs with a relatively large Schottky barrier for injection, the situation is different as can be seen in Fig. 4.20b, which shows the potential profiles taken of a P3HT transistor with Cr electrodes. They show pronounced asymmetry between the source and drain, i.e., a considerably larger voltage is needed to inject the holes at the source than to extract them at the drain ($\Delta V_s > \Delta V_d$). And this asymmetry is not due to one of the two electrodes forming better contact with the polymer than the other, since upon switching the source and drain electrodes, nearly identical result can be verified by comparing the 300 K profile in Fig. 4.20b with the profile in the inset.

Charge carriers trapped in polystyrene (PS) were investigated with KPFM [70]. Lateral heterojunctions of pentacene/PS were scanned using KPFM, as shown in Fig. 4.21a, exhibiting polarization along a side view of a lateral nonvolatile organic field effect transistor (OFET) dielectric interface. Figure 4.21b shows

Fig. 4.20 Profiles of the electrostatic potential across the channel of operating transistors. (a) P3HT transistor with Cr–Au source/drain electrodes ($L \approx 5.3 \mu\text{m}$, $V_g = -20 \text{ V}$, $V_d = -8 \text{ V}$). (b) Profiles of an $L \approx 5.5 \mu\text{m}$ P3HT transistor with Cr electrodes taken at three different temperatures ($V_g = -40 \text{ V}$, $V_d = -8 \text{ V}$). The inset of (b) shows a profile obtained after switching the source and drain on the same TFT ($V_g = -40 \text{ V}$, $V_d = -8 \text{ V}$) (Reprinted with permission from [69]. Copyright (2003), AIP Publishing LLC)



KPFM line scans which were performed on the samples as the bias applied to the pentacene was varied, showing the potential drop across pentacene, PS, and the interface. Figure 4.21c illustrates the measured surface potential after the sample being charged at +200 V to pentacene for 10 min. Before charging, the surface potential on the pentacene side can be raised to higher value than the PS side by applying a small voltage, while after being charged at +200 V, the surface potential on the PS side remains higher than that on the pentacene side, indicating that charges are injected into the PS dielectric layer from the pentacene. When replacing pentacene with gold, a greater shift in surface potential can be observed, due to the higher conductivity of gold compared to pentacene. The charged samples have an offset difference in surface potential when compared to uncharged samples. This offset in surface potential is a result of the stored charges in the PS layers.

Carbon nanotubes (CNTs) have attracted much attention for their unique properties and numerous demonstrations of FETs based on semiconducting CNTs have been reported [71, 72]. KPFM has been applied to study FETs at different bias voltage. Surface potentials along a SWCNT in FETs were studied [73]. The gradual changes in contrast along the SWCNT bundle indicate the current flowing between the two electrodes. The fact that the potential was partially increased by applying a gate bias voltage indicates that the bundle probably includes semiconducting-like nanotubes in addition to metallic ones in this region. When the CNTFET is in the ON state, it shows uniform potential distribution along the CNT. However, when the CNTFET is in the OFF state, nonuniform potential image with dark spots is obtained, probably due to the defects in the CNTs [74].

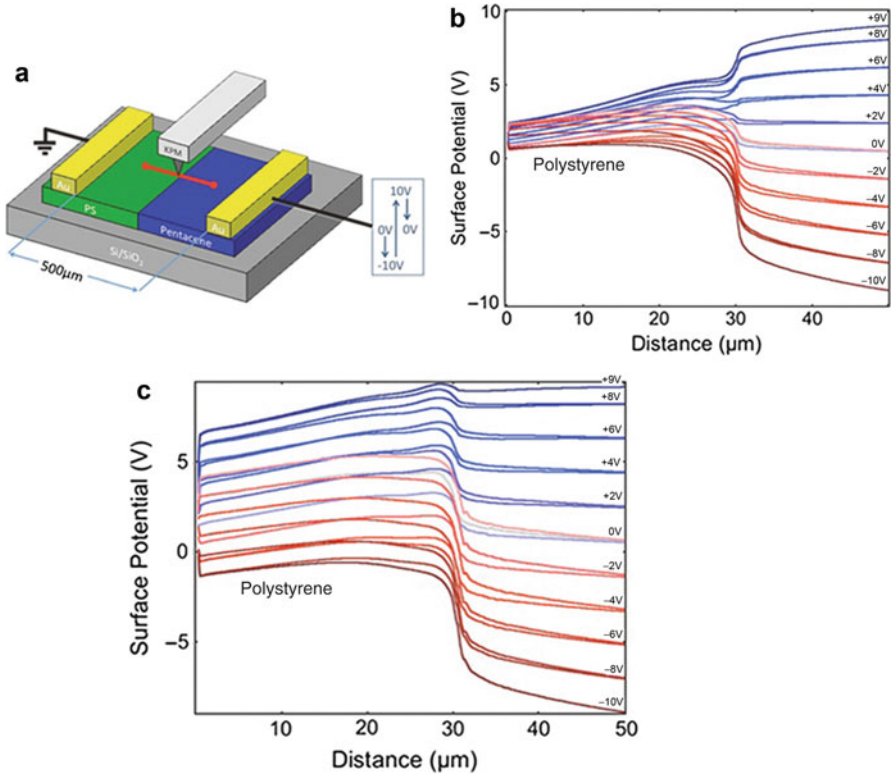


Fig. 4.21 (a) The schematic of the heterojunction. (b) The uncharged sample surface potential at various applied biases. The sample was initially scanned in the negative direction to -10 V and then the bias was stepped up to $+9$ V and finally back to 0 V. (c) The sample was removed from the KPFM and charged at $+200$ V for 10 min and then returned to the KPFM and rescanned (Reprinted with permission from [70]. Copyright (2012), AIP Publishing LLC)

Contact resistance of individual Cr–Au electrodes contacting graphene in a graphene device was studied using KPFM [11]. Figure 4.22a shows the current (I) versus V_{SD} characteristics at a fixed gate voltage. The slope of I – V_{SD} yields a resistance of 3.44 k Ω , which includes the contributions of contact resistances between each electrode and the graphene channel. As shown in Fig. 4.22b, the surface potential of the biased drain electrode shifts upward as V_{SD} increases, as drain electrode was grounded. From Fig. 4.22c, linearly increasing V_{CPD} in the channel and kinks in V_{CPD} at the junctions can be found. These sudden potential drops are attributed to the contact resistance between the electrodes and graphene. The vertical ratios between the kinks and the slope correspond to the source and drain contact resistances (r_s and r_d) and graphene channel resistance (r_c). Considering the total resistance of this device is 3.44 k Ω , $r_d : r_c : r_s = 0.5 : 1.7 : 1.24$ k Ω is obtained.

KPFM can also be used to study the interlayer screening effect of graphene sheets in graphene-based FETs [75]. The surface potential decreases exponentially

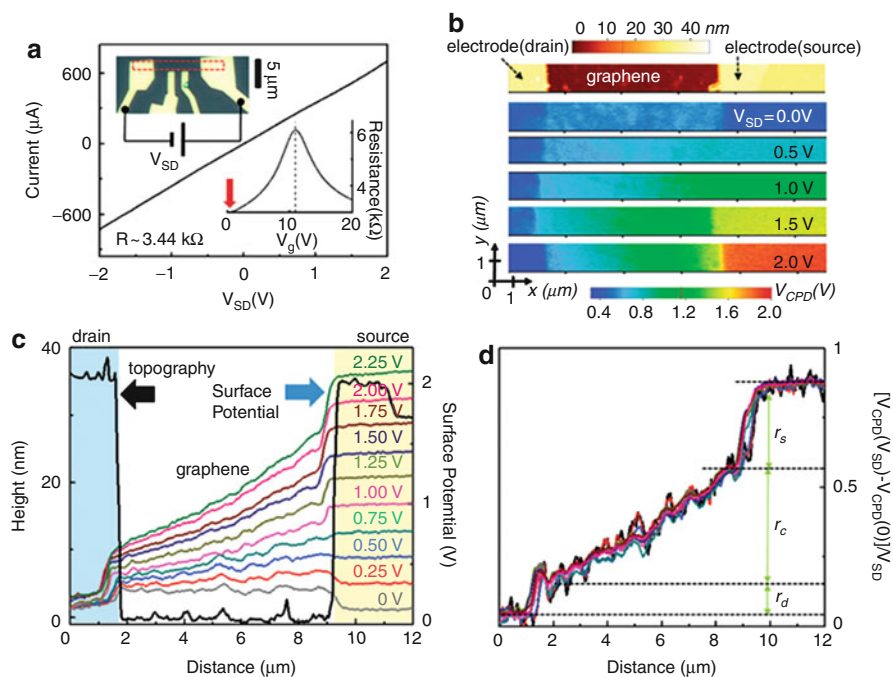


Fig. 4.22 (a) Current (I) and bias voltage (V_{SD}) characteristic of a SLG device. *Upper inset* shows the optical microscope image of the device. *Lower inset* shows the resistance as a function of V_g . The *vertical arrow* indicates the gate voltages and *dotted line*, V_D . (b) Topographic image (*top*) and surface potential images of the area marked by the rectangular box in (a). The drain electrode is grounded, while the source electrode is biased by V_{SD} as indicated in each panel. The gate voltage is fixed to $V_g = 0$. (c) Surface potential profiles at different V_{SD} . (d) Normalized and referenced surface potential profiles shown in (c) (Reprinted with permission from [11]. Copyright (2009) American Chemical Society)

with the number of layers, demonstrating the graphene independently screens the surface potential layer by layer.

6.5 Atomic Resolution KPFM

In atomically resolved KPFM, the measured CPD is defined as local contact potential difference (LCPD), which depends on the electrostatic interaction on an atomic scale. The LCPD is based on the Wandelt's concept of a local work function, which illustrates the short-ranged atomic-scale variation of work function on surfaces [76, 77]. Similar to the local work function concept, atomic-scale KPFM measurements of the total electrostatic force include a new term (a bias-dependent short-range force), which induces the atomic LCPD contrast. The atomic-scale contrast of CPD is attributed to a short-range force, due to the microscopic interaction between the apex of the tip and surface atoms.

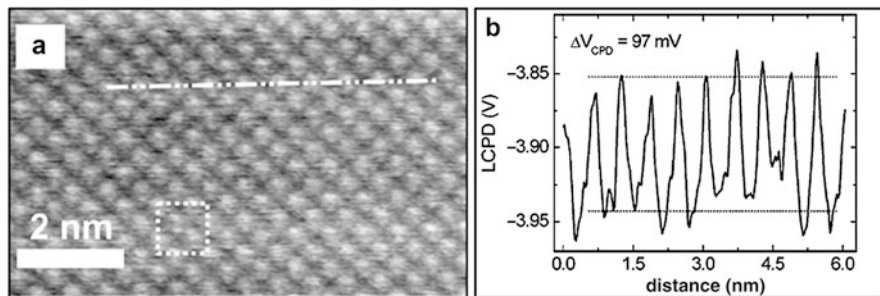


Fig. 4.23 (a) CPD image of KBr (001) surface by KPFM. (b) CPD profile along the *dashed line* in (a) (Reprinted with permission from [78]. Copyright (2008) by the American Physical Society)

Atomic resolution KPFM results of KBr (001) surface in UHV were obtained [78]. As shown in Fig. 4.23, the image exhibits atomic features, the measured period of which is 0.63 nm, which is visible in the joint cross section. This value is in good agreement with the lattice constant of KBr, 0.66 nm. The vertical contrast yields about 100 mV between K^+ and Br^- around an average value of -3.9 V. The expression of the electrostatic force can be split into two major contributions: the first stands for the coupling between the microscopic structure of the tip apex and the capacitor formed between the tip, the ionic crystal, and the counter electrode, while the second term depicts the influence of the Madelung surface potential on the mesoscopic part of the tip, independent of its microscopic structure. The former has the lateral periodicity of the Madelung surface potential, whereas the latter only acts as a static component and shifts the total force. Beyond the dielectric properties of the crystal, the ionic polarization of the sample resulting from the influence of the tip/counter electrode capacitor is responsible for the atomic contrast of the KPFM signal.

Sub-nanometer resolution LCPD has also been observed on a variety of surfaces including Si [79–83], TiO_2 [84], and InSb [26]. Atomic-scale variations in the electronic surface potential on TiO_2 (110) surface were studied [84]. As shown in Fig. 4.24a, the dark-bright striped pattern visibly reflects the normal appearance of the TiO_2 (1×1) surface, with alternating rows of bridging oxygen atoms [O(2c)] and in-plane titanium atoms [Ti(5c)], which are also observed in LCPD image, suggesting the KPFM setup is able to detect atomic-scale variation in the surface charge densities. In LCPD image, the dark rows (more negative) are assigned to O (2c) rows, and those bright are assigned to Ti(5c) rows. This identification is also supported by the topography image (Fig. 4.24a), where the contrast is observed to be reversed. The results confirm the concepts applied for the interpretation of the LCPD image and furthermore demonstrate that LCPD images can be used for a chemical identification of the surface structure.

KPFM can be used to distinguish atom charge state [85] and measure the charge distribution within single molecules [86–88]. KPFM can be used to detect charge states of metallic atoms by measuring the LCPD between metallic and substrate [85]. The local contact potential difference is shifted depending

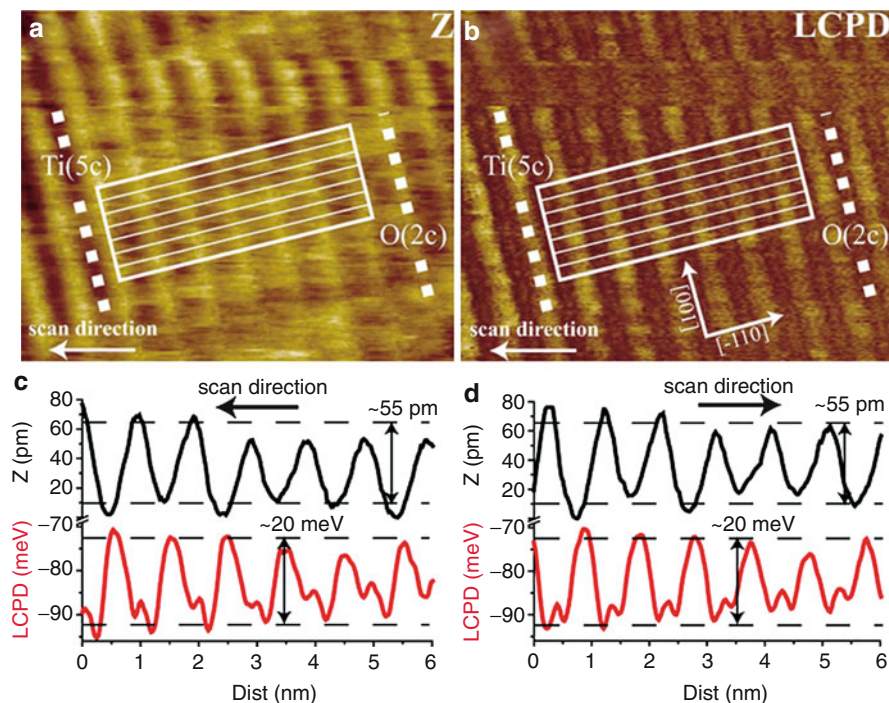


Fig. 4.24 (a) The AFM topography image (Z). (b) Simultaneously recorded LCPD. (c) The 99-line average twin cross sections of Z and LCPD, as indicated by the *white boxes* in (a) and (b). (d) The 99-line average twin cross sections of Z and LCPD recorded in the forward fast-scan direction (Reprinted with permission from [84]. Copyright (2008) by the American Physical Society)

on the sign of the charge and allows the discrimination of positively charged, neutral, and negatively charged atoms.

Charge distribution within naphthalocyanine molecules, which have been reported as molecular switches [89], on a thin insulating layer of NaCl on Cu (111), was studied using KPFM [87]. Figure 4.25b and c shows the LCPD images recorded before and after switching the tautomerization state of a single naphthalocyanine molecule. An obvious asymmetry between the H-lobes and the N-lobes can be observed, with greater values of V^* above the N-lobes. The asymmetry is even more clearly visible in the difference image (Fig. 4.25d) obtained by subtracting the LCPD images of the initial and switched configurations. The DFT-calculated results (Fig. 4.25e) reveal that the submolecular resolution in the LCPD images reflects the total charge distribution within the molecule.

In this chapter, various aspects of KPFM including theory, instrumentation (AM and FM mode), and application have been discussed. KPFM is a powerful technique for high spatial resolution electrical property measurement and has shown to be a feasible method widely applicable in nanoscience and nanotechnology.

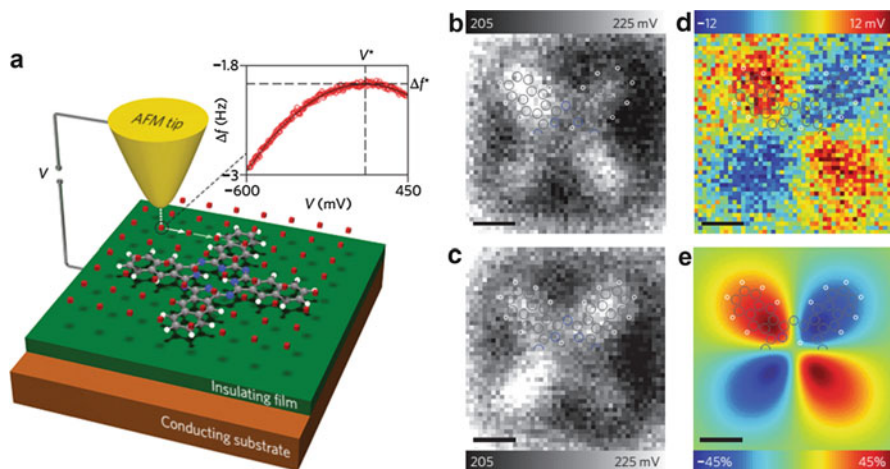


Fig. 4.25 LCPD images of the tautomerization switching of naphthalocyanine. **(a)** Schematic of the measurement principle. **(b)** and **(c)**, LCPD images of naphthalocyanine before **(b)** and after **(c)** switching the tautomerization state of the molecule. **(d)** Difference image obtained by subtracting **(c)** from **(b)**. **(e)** DFT-calculated asymmetry of the z -component of the electric field above a free naphthalocyanine molecule at a distance $d = 0.5$ nm from the molecular plane (Reprinted by permission from Macmillan Publishers Ltd: Nat Nanotechnol [87], copyright (2012))

References

1. Kelvin L (1898) V. contact electricity of metals. London, Edinburgh, Dublin Philos Mag J Sci 46(278):82–120
2. Zisman W (1932) A new method of measuring contact potential differences in metals. Rev Sci Instrum 3(7):367–370
3. Melitz W, Shen J, Kummel AC, Lee S (2011) Kelvin probe force microscopy and its application. Surf Sci Rep 66(1):1–27
4. Sadewasser S, Glatzel T (2012) Kelvin probe force microscopy. Springer, Heidelberg
5. Nonnenmacher M, O’Boyle M, Wickramasinghe H (1991) Kelvin probe force microscopy. Appl Phys Lett 58:2921
6. O’Boyle M, Hwang T, Wickramasinghe H (1999) Atomic force microscopy of work functions on the nanometer scale. Appl Phys Lett 74(18):2641–2642
7. Yamauchi T, Tabuchi M, Nakamura A (2004) Size dependence of the work function in Inas quantum dots on Gaas (001) as studied by Kelvin force probe microscopy. Appl Phys Lett 84(19):3834–3836
8. Ziegler D, Gava P, Güttinger J, Molitor F, Wirtz L, Lazzeri M, Saitta A, Stemmer A, Mauri F, Stampfer C (2011) Variations in the work function of doped single- and few-layer graphene assessed by Kelvin probe force microscopy and density functional theory. Phys Rev B 83(23):235434
9. Sun H, Chu H, Wang J, Ding L, Li Y (2010) Kelvin probe force microscopy study on nanotriboelectrification. Appl Phys Lett 96(8):083112–083112-3
10. Liu L, Li G (2010) Electrical characterization of single-walled carbon nanotubes in organic solar cells by Kelvin probe force microscopy. Appl Phys Lett 96:083302
11. Yu Y-J, Zhao Y, Ryu S, Brus LE, Kim KS, Kim P (2009) Tuning the graphene work function by electric field effect. Nano Lett 9(10):3430–3434

12. Colchero J, Gil A, Baró A (2001) Resolution enhancement and improved data interpretation in electrostatic force microscopy. *Phys Rev B* 64(24):245403
13. Zerweck U, Loppacher C, Otto T, Grafström S, Eng LM (2005) Accuracy and resolution limits of Kelvin probe force microscopy. *Phys Rev B* 71(12):125424
14. Jacobs H, Leuchtmann P, Homan O, Stemmer A (1998) Resolution and contrast in Kelvin probe force microscopy. *J Appl Phys* 84(3):1168–1173
15. Ding L, Li Y, Chu H, Li C, Yang Z, Zhou W, Tang ZK (2007) High speed atomic force microscope lithography driven by electrostatic interaction. *Appl Phys Lett* 91(2):023121–023121-3
16. Mesquida P, Stemmer A (2001) Attaching silica nanoparticles from suspension onto surface charge patterns generated by a conductive atomic force microscope tip. *Adv Mater* 13(18):1395–1398
17. Lee G, Shin Y-H, Son JY (2009) Formation of self-assembled polyelectrolyte multilayer nanodots by scanning probe microscopy. *J Am Chem Soc* 131(5):1634–1635
18. Seemann L, Stemmer A, Naujoks N (2007) Local surface charges direct the deposition of carbon nanotubes and fullerenes into nanoscale patterns. *Nano Lett* 7(10):3007–3012
19. Palleau E, Sangeetha NM, Viau G, Marty J-D, Ressler L (2011) Coulomb force directed single and binary assembly of nanoparticles from aqueous dispersions by Afm nanoxerography. *ACS Nano* 5(5):4228–4235
20. Yue S, Xueqiang Z, Ying W, Xuejiao Z, Jun H, Shouwu G, Yi Z (2013) Charge transfer between reduced graphene oxide sheets on insulating substrates. *Appl Phys Lett* 103(5):053107 (4 pp)–053107 (4 pp)
21. Verdaguer A, Cardellach M, Segura J, Sacha G, Moser J, Zdrojek M, Bachtold A, Fraxedas J (2009) Charging and discharging of graphene in ambient conditions studied with scanning probe microscopy. *Appl Phys Lett* 94(23):233105–233105-3
22. Moser J, Verdaguer A, Jimenez D, Barreiro A, Bachtold A (2008) The environment of graphene probed by electrostatic force microscopy. *Appl Phys Lett* 92(12):123507–123507-3
23. Guo LQ, Zhao XM, Bai Y, Qiao LJ (2012) Water adsorption behavior on metal surfaces and its influence on surface potential studied by in situ Spm. *Appl Surf Sci* 258(22):9087–9091
24. Craig PP, Radeka V (1970) Stress dependence of contact potential: the Ac Kelvin method. *Rev Sci Instrum* 41(2):258–264
25. Goryl M, Kolodziej J, Krok F, Piatkowski P, Such B, Szymonski M (2005) Epitaxial nanostructures assembled on Insb (001) by submonolayer deposition of gold. *Microelec Eng* 81(2):394–399
26. Krok F, Sajewicz K, Konior J, Goryl M, Piatkowski P, Szymonski M (2008) Lateral resolution and potential sensitivity in Kelvin probe force microscopy: towards understanding of the sub-nanometer resolution. *Phys Rev B* 77(23):235427
27. Shusterman S, Raizman A, Sher A, Paltiel Y, Schwarzman A, Lepkifker E, Rosenwaks Y (2007) Nanoscale mapping of strain and composition in quantum dots using Kelvin probe force microscopy. *Nano Lett* 7(7):2089–2093
28. Wang QH, Kalantar-Zadeh K, Kis A, Coleman JN, Strano MS (2012) Electronics and optoelectronics of two-dimensional transition metal dichalcogenides. *Nat Nanotechnol* 7(11):699–712
29. Xu M, Liang T, Shi M, Chen H (2013) Graphene-like two-dimensional materials. *Chem Rev* 113(5):3766–3798
30. Li Y, Xu C-Y, Zhen L (2013) Surface potential and interlayer screening effects of few-layer Mos 2 nanoflakes. *Appl Phys Lett* 102(14):143110–143110-4
31. Datta SS, Strachan DR, Mele EJ, Johnson ATC (2009) Surface potentials and layer charge distributions in few-layer graphene films. *Nano Lett* 9(1):7–11
32. Jaafar M, López-Polín G, Gómez-Navarro C, Gómez-Herrero J (2012) Step like surface potential on few layered graphene oxide. *Appl Phys Lett* 101(26):263109
33. Ago H, Kugler T, Cacialli F, Salaneck WR, Shaffer MS, Windle AH, Friend RH (1999) Work functions and surface functional groups of multiwall carbon nanotubes. *J Phys Chem B* 103(38):8116–8121

34. Shiraishi M, Ata M (2001) Work function of carbon nanotubes. *Carbon* 39(12):1913–1917
35. Suzuki S, Bower C, Watanabe Y, Zhou O (2000) Work functions and valence band states of pristine and Cs-intercalated single-walled carbon nanotube bundles. *Appl Phys Lett* 76(26):4007–4009
36. Spadafora EJ, Saint-Aubin K, Celle C, Demadrille R, Grévin B, Simonato J-P (2012) Work function tuning for flexible transparent electrodes based on functionalized metallic single walled carbon nanotubes. *Carbon* 50(10):3459–3464
37. Martel RA, Schmidt T, Shea H, Hertel T, Avouris P (1998) Single-and multi-wall carbon nanotube field-effect transistors. *Appl Phys Lett* 73:2447
38. Tans SJ, Verschueren AR, Dekker C (1998) Room-temperature transistor based on a single carbon nanotube. *Nature* 393(6680):49–52
39. Derycke V, Martel R, Appenzeller J, Avouris P (2001) Carbon nanotube inter-and intramolecular logic gates. *Nano Lett* 1(9):453–456
40. Derycke V, Martel R, Appenzeller J, Avouris P (2002) Controlling doping and carrier injection in carbon nanotube transistors. *Appl Phys Lett* 80:2773
41. Cui X, Freitag M, Martel R, Brus L, Avouris P (2003) Controlling energy-level alignments at carbon nanotube/Au contacts. *Nano Lett* 3(6):783–787
42. Filletter T, Emtsev K, Seyller T, Bennewitz R (2008) Local work function measurements of epitaxial graphene. *Appl Phys Lett* 93(13):133117–133117-3
43. Casiraghi C, Pisana S, Novoselov K, Geim A, Ferrari A (2007) Raman fingerprint of charged impurities in graphene. *Appl Phys Lett* 91(23):233108–233108-3
44. Yan J, Henriksen EA, Kim P, Pinczuk A (2008) Observation of anomalous phonon softening in bilayer graphene. *Phys Rev Lett* 101(13):136804
45. Yan J, Zhang Y, Kim P, Pinczuk A (2007) Electric field effect tuning of electron–phonon coupling in graphene. *Phys Rev Lett* 98(16):166802
46. Shi Y, Kim KK, Reina A, Hofmann M, Li L-J, Kong J (2010) Work function engineering of graphene electrode via chemical doping. *ACS Nano* 4(5):2689–2694
47. Wang R, Wang S, Zhang D, Li Z, Fang Y, Qiu X (2010) Control of carrier type and density in exfoliated graphene by interface engineering. *ACS Nano* 5(1):408–412
48. Bußmann BK, Ochedowski O, Schleberger M (2011) Doping of graphene exfoliated on SrTiO₃. *Nanotechnology* 22(26):265703
49. Wang X, Xu J-B, Xie W, Du J (2011) Quantitative analysis of graphene doping by organic molecular charge transfer. *J Phys Chem C* 115(15):7596–7602
50. Pearce R, Eriksson J, Iakimov T, Hultman L, Lloyd Spetz PA, Yakimova R (2013) On the differing sensitivity to chemical gating of single and double layer epitaxial graphene explored using scanning Kelvin probe microscopy. *ACS Nano* 7:4647–4656
51. Zhou X, He S, Brown KA, Mendez-Arroyo J, Boey F, Mirkin CA (2013) Locally altering the electronic properties of graphene by nanoscopically doping it with rhodamine 6 g. *Nano Lett* 13(4):1616–1621
52. Sque SJ, Jones R, Briddon PR (2007) The transfer doping of graphite and graphene. *Phys Status Solidi (a)* 204(9):3078–3084
53. Cherniavskaya O, Chen L, Islam MA, Brus L (2003) Photoionization of individual CdSe/Cds core/shell nanocrystals on silicon with 2-Nm oxide depends on surface band bending. *Nano Lett* 3(4):497–501
54. Ludeke R, Cartier E (2001) Imaging of trapped charge in SiO₂ and at the SiO₂–Si interface. *Appl Phys Lett* 78(25):3998–4000
55. Linsebigler AL, Lu G, Yates JT Jr (1995) Photocatalysis on TiO₂ surfaces: principles, mechanisms, and selected results. *Chem Rev* 95(3):735–758
56. Sasahara A, Pang CL, Onishi H (2006) Probe microscope observation of platinum atoms deposited on the TiO₂ (110)-(1 × 1) surface. *J Phys Chem B* 110(27):13453–13457
57. Sasahara A, Pang CL, Onishi H (2006) Local work function of Pt clusters vacuum-deposited on a TiO₂ surface. *J Phys Chem B* 110(35):17584–17588

58. Haruta M, Yamada N, Kobayashi T, Iijima S (1989) Gold catalysts prepared by coprecipitation for low-temperature oxidation of hydrogen and of carbon monoxide. *J Catal* 115(2):301–309
59. Chung HJ, Yurtsever A, Sugimoto Y, Abe M, Morita S (2011) Kelvin probe force microscopy characterization of TiO₂ (110)-supported Au clusters. *Appl Phys Lett* 99(12):123102
60. Kim JY, Lee K, Coates NE, Moses D, Nguyen T-Q, Dante M, Heeger AJ (2007) Efficient tandem polymer solar cells fabricated by all-solution processing. *Science* 317(5835):222–225
61. Li G, Shrotriya V, Huang J, Yao Y, Moriarty T, Emery K, Yang Y (2005) High-efficiency solution processable polymer photovoltaic cells by self-organization of polymer blends. *Nat Mater* 4(11):864–868
62. Yu G, Gao J, Hummelen JC, Wudl F, Heeger AJ (1995) Polymer photovoltaic cells – enhanced efficiencies via a network of internal donor-acceptor heterojunctions. *Science* 270(5243):1789–1791
63. Li C, Chen Y, Wang Y, Iqbal Z, Chhowalla M, Mitra S (2007) A fullerene–single wall carbon nanotube complex for polymer bulk heterojunction photovoltaic cells. *J Mater Chem* 17(23):2406–2411
64. Liu L, Stanchina WE, Li G (2009) Effects of semiconducting and metallic single-walled carbon nanotubes on performance of bulk heterojunction organic solar cells. *Appl Phys Lett* 94(23):233309–233309-3
65. Kymakis E, Alexandrou I, Amaratunga G (2003) High open-circuit voltage photovoltaic devices from carbon-nanotube-polymer composites. *J Appl Phys* 93(3):1764–1768
66. Ren S, Bernardi M, Lunt RR, Bulovic V, Grossman JC, Gradecak S (2011) Toward efficient carbon nanotube/P3ht solar cells: active layer morphology, electrical, and optical properties. *Nano Lett* 11(12):5316–5321
67. Lan F, Li G (2013) Direct observation of hole transfer from semiconducting polymer to carbon nanotubes. *Nano Lett* 13(5):2086–2091
68. Dimitrakopoulos CD, Malenfant PR (2002) Organic thin film transistors for large area electronics. *Adv Mater* 14(2):99–117
69. Burgi L, Richards T, Friend R, Sirringhaus H (2003) Close look at charge carrier injection in polymer field-effect transistors. *J Appl Phys* 94(9):6129–6137
70. Dawidczyk T, Johns G, Ozgun R, Alley O, Andreou A, Markovic N, Katz H (2012) Kelvin probe microscopic visualization of charge storage at polystyrene interfaces with pentacene and gold. *Appl Phys Lett* 100(7):073305
71. Avouris P (2002) Carbon nanotube electronics. *Chem Phys* 281(2):429–445
72. McEuen PL, Fuhrer MS, Park H (2002) Single-walled carbon nanotube electronics. *Nanotechnol, IEEE Trans* 1(1):78–85
73. Miyato Y, Kobayashi K, Matsushige K, Yamada H (2007) Surface potential investigation on single wall carbon nanotubes by Kelvin probe force microscopy and atomic force microscope potentiometry. *Nanotechnology* 18(8):084008
74. Okigawa Y, Umesaka T, Ohno Y, Kishimoto S, Mizutani T (2008) Potential profile measurement of carbon nanotube fet's based on the electrostatic force detection. *Nano* 3(01):51–54
75. Lee N, Yoo J, Choi Y, Kang C, Jeon D, Kim D, Seo S, Chung H (2009) The interlayer screening effect of graphene sheets investigated by Kelvin probe force microscopy. *Appl Phys Lett* 95(22):222107–222107-3
76. Küppers J, Wandelt K, Ertl G (1979) Influence of the local surface structure on the 5p photoemission of adsorbed xenon. *Phys Rev Lett* 43(13):928
77. Wandelt K (1997) The local work function: concept and implications. *Appl Surf Sci* 111:1–10
78. Bocquet F, Nony L, Loppacher C, Glatzel T (2008) Analytical approach to the local contact potential difference on (001) ionic surfaces: implications for Kelvin probe force microscopy. *Phys Rev B* 78(3):035410
79. Arai T, Tomitori M (2004) Observation of electronic states on Si (111)-(7 × 7) through short-range attractive force with noncontact atomic force spectroscopy. *Phys Rev Lett* 93(25):256101

80. Kitamura S, Iwatsuki M (1998) High-resolution imaging of contact potential difference with ultrahigh vacuum noncontact atomic force microscope. *Appl Phys Lett* 72(24):3154–3156
81. Kitamura SI, Suzuki K, Iwatsuki M, Mooney C (2000) Atomic-scale variations in contact potential difference on Au/Si (111) 7×7 surface in ultrahigh vacuum. *Appl Surf Sci* 157(4):222–227
82. Okamoto K, Sugawara Y, Morita S (2002) The elimination of the ‘Artifact’ in the electrostatic force measurement using a novel noncontact atomic force microscope/electrostatic force microscope. *Appl Surf Sci* 188(3):381–385
83. Okamoto K, Yoshimoto K, Sugawara Y, Morita S (2003) Kpfm imaging of Si(111)5 root 3×5 root 3-Sb surface for atom distinction using Nc-Afm. *Appl Surf Sci* 210(1–2):128–133
84. Enevoldsen GH, Glatzel T, Christensen MC, Lauritsen JV, Besenbacher F (2008) Atomic scale Kelvin probe force microscopy studies of the surface potential variations on the Tio(2) (110) surface. *Phys Rev Lett* 100(23):236104
85. Gross L, Mohn F, Liljeroth P, Repp J, Giessibl FJ, Meyer G (2009) Measuring the charge state of an adatom with noncontact atomic force microscopy. *Science* 324(5933):1428–1431
86. Leoni T, Guillermet O, Walch H, Langlais V, Scheuermann A, Bonvoisin J, Gauthier S (2011) Controlling the charge state of a single redox molecular switch. *Phys Rev Lett* 106(21):216103
87. Mohn F, Gross L, Moll N, Meyer G (2012) Imaging the charge distribution within a single molecule. *Nat Nanotechnol* 7(4):227–231
88. Walch H, Leoni T, Guillermet O, Langlais V, Scheuermann A, Bonvoisin J, Gauthier S (2012) Electromechanical switching behavior of individual molecular complexes of Cu and Ni on NaCl-covered Cu (111) and Ag (111). *Phys Rev B* 86(7):075423
89. Liljeroth P, Repp J, Meyer G (2007) Current-induced hydrogen tautomerization and conductance switching of naphthalocyanine molecules. *Science* 317(5842):1203–1206